



## Article

# Multi-Proxy Provenance Analyses of the Kingriali and Datta Formations (Triassic–Jurassic Transition): Evidence for Westward Extension of the Neo-Tethys Passive Margin from the Salt Range (Pakistan)

Shahid Iqbal <sup>1,2,\*</sup> , Michael Wagreich <sup>2</sup>, Mehwish Bibi <sup>2</sup>, Irfan U. Jan <sup>3</sup> and Susanne Gier <sup>2</sup> 

- <sup>1</sup> Department of Earth Sciences, Quaid-i-Azam University, Islamabad 45320, Pakistan  
<sup>2</sup> Department of Geology, University of Vienna, Althanstrasse 14, A-1090 Vienna, Austria; michael.wagreich@univie.ac.at (M.W.); bibimehwish15@gmail.com (M.B.); susanne.gier@univie.ac.at (S.G.)  
<sup>3</sup> National Centre for Excellence in Geology, University of Peshawar, Peshawar 25130, Khyber Pakhtunkhwa, Pakistan; irfanjan6@gmail.com  
\* Correspondence: siqbal@qau.edu.pk



**Citation:** Iqbal, S.; Wagreich, M.; Bibi, M.; Jan, I.U.; Gier, S. Multi-Proxy Provenance Analyses of the Kingriali and Datta Formations (Triassic–Jurassic Transition): Evidence for Westward Extension of the Neo-Tethys Passive Margin from the Salt Range (Pakistan). *Minerals* **2021**, *11*, 573. <https://doi.org/10.3390/min11060573>

Academic Editors:  
Hans-Jürgen Gawlick,  
Michał Krobicki and Laszlo Bujtor

Received: 24 April 2021  
Accepted: 22 May 2021  
Published: 27 May 2021

**Publisher's Note:** MDPI stays neutral with regard to jurisdictional claims in published maps and institutional affiliations.



**Copyright:** © 2021 by the authors. Licensee MDPI, Basel, Switzerland. This article is an open access article distributed under the terms and conditions of the Creative Commons Attribution (CC BY) license (<https://creativecommons.org/licenses/by/4.0/>).

**Abstract:** The Salt Range, in Pakistan, preserves an insightful sedimentary record of passive margin dynamics along the NW margin of the Indian Plate during the Mesozoic. This study develops provenance analyses of the Upper Triassic (Kingriali Formation) to Lower Jurassic (Datta Formation) siliciclastics from the Salt and Trans Indus ranges based on outcrop analysis, petrography, bulk sediment elemental geochemistry, and heavy-mineral data. The sandstones are texturally and compositionally mature quartz arenites and the conglomerates are quartz rich oligomictic conglomerates. Geochemical proxies support sediment derivation from acidic sources and deposition under a passive margin setting. The transparent heavy mineral suite consists of zircon, tourmaline, and rutile (ZTR) with minor staurolite in the Triassic strata that diminishes in the Jurassic strata. Together, these data indicate that the sediments were supplied by erosion of the older siliciclastics of the eastern Salt Range and adjoining areas of the Indian Plate. The proportion of recycled component exceeds the previous literature estimates for direct sediment derivation from the Indian Shield. A possible increase in detritus supply from the Salt Range itself indicates notably different conditions of sediment generation, during the Triassic–Jurassic transition. The present results suggest that, during the Triassic–Jurassic transition in the Salt Range, direct sediment supply from the Indian Shield was probably reduced and the Triassic and older siliciclastics were exhumed on an elevated passive margin and reworked by a locally established fluvio-deltaic system. The sediment transport had a north-northwestward trend parallel to the northwestern Tethyan margin of the Indian Plate and normal to its opening axis. During the Late Triassic, hot and arid hot-house palaeoclimate prevailed in the area that gave way to a hot and humid greenhouse palaeoclimate across the Triassic–Jurassic Boundary. Sedimentological similarity between the Salt Range succession and the Neo-Tethyan succession exposed to the east on the northern Indian passive Neo-Tethyan margin suggests a possible westward extension of this margin.

**Keywords:** Triassic–Jurassic boundary; framework mineralogy; sediment geochemistry; heavy minerals; passive margin; Neo-Tethys opening; Himalayas; Salt Range

## 1. Introduction

Pangaea break-up resulted in the formation of rift systems and consecutive passive margins [1–3] associated with globally distributed extensional structures, rift basins, breakup, and passive margins [4–7]. The Triassic–Jurassic Boundary (TJB) marks one of the five major Phanerozoic mass extinction intervals [8] and a short-lived, but pronounced

sea-level fall is globally observed during this time interval [9,10]. This sea-level fall exposed new areas for mechanical denudation and chemical weathering, e.g., in England [11], Germany, Danish Basin, Sweden, Poland, Austria, Hungary, and Slovakia [12–15], and provided new siliciclastic supplies for rift basins and passive margins.

The geologic evolution of the northern margin of the Indian Plate is best recorded in the stratigraphy of the Tethys Himalayan Succession (THS) e.g., [16]. The E/W-trending THS stretch along the Himalayan Orogen for over 1500 km, from NW India in the west to Nepal and southern Tibet in the east [17–19]. The THS preserves a continuous stratigraphic record from Late Precambrian to Eocene, thereby documenting the history of northern Indian margin during most of the Phanerozoic [20–29]. The Neo-Tethys opening is well-documented by sedimentary records in Spiti, Lahaul, Zaskar, and adjoining areas of Kashmir e.g., [30–33]. The Salt and Trans Indus ranges of the NW Pakistan (Figures 1 and 2) preserve Precambrian to Recent sedimentary successions [34–40]. The Salt Range Succession (SRS) displays an apparent lithological correlation with the THS exposed in the Lahul-Zaskar and the nearby Kashmir area (Table 1). This may help in tracing the Neo-Tethyan margin of the Greater India further to the west. The SRS has widely been investigated for the reconstruction of the geological history of sediment generation sites, palaeoclimatic conditions, transport pathways, and depositional sites e.g., [40–45]. However, most of such provenance studies conclude with sediment derivation from the Indian Plate basement rocks and the hypothesis of possible link between the SRS and the THS remains yet to be tested.

The present work analyses siliciclastics of the upper Triassic Kingriali Formation to the Lower Jurassic Datta Formation, using outcrop analysis, petrographic data, bulk rock geochemistry, and heavy mineral data. Based on these data, we propose a source-to-sink history of the Salt and Trans Indus ranges following the demise of the Rhaetian carbonate platform. The present results indicate that the conventional Indian Plate basement rocks may not have served as direct sources for the siliciclastics of the Salt Range around the TJB interval. Instead, the source area was located on the elevated NW-passive margin of the Indian Plate facing the southern Neo-Tethys. Exhumation of the passive margin possibly exposed the eastern Salt Range and areas further to the east, thereby generating new siliciclastic source areas. This passive margin setting in the Salt Range during the TJB interval could represent a westward extension of the NW-passive margin of the Greater India.

**Table 1.** Similarities between the Tethyan Himalaya Succession (THS) and Salt Range Succession (SRS) and their potential link to the Neo-Tethys tectonic events [16,20–24,37].

Episode	Tethyan Himalaya Succession (THS)	Salt Range Succession (SRS)
Syn-Collisional	Paleogene limestones followed by post Eocene fluvio-deltaic red beds derived from erosion of the Himalayas	Paleogene shallow marine limestones and shales followed by Post Eocene brown-red fluvio-deltaic siliciclastics derived from erosion of Himalayas
Drift	(g) Cretaceous drowning and deposition of glauconitic and phosphatic ironstones. (f) Middle Jurassic carbonate-platform sedimentation became widespread (“mature passive-margin stage”) (e) Early Jurassic development of dysoxic bottom waters (d) Late Triassic-Lower Jurassic quartzose sands deposition (locally until the middle Early Jurassic) (c) Norian sudden increase in siliciclastic detritus suddenly (Passive margin rejuvenation) (b) Lower Triassic deep-water, ammonoid-bearing sediment deposition (a) Upper Permian transgressive bioclastic sands and shales with deepening upward trend	(g) Cretaceous iron rich glauconitic shales and sandstones (Chichali and Lumshiwal formations) (f) Middle Jurassic widespread platform carbonates deposition (Samana Suk Formation) (e) Toarcian black shale deposition (Shinawari Formation) (d) Late Triassic shale and sandstone (Kingriali Formation) and thick lower Jurassic quartzose sandstones Datta Formation) (c) Middle Triassic thick sandstones with large scale slumps (Tredian Formation) pointing to passive margin rejuvenation (b) Lower Triassic deep marine ammonoid rich deposition (Mianwali Formation) (a) Upper Permian sandstones and shales (Warchha and Sardhai formations) followed by thick, richly fossiliferous carbonates (Zaluch Group)
Syn-Rift	Lowermost Permian glaciogenic diamictites overlain by Sakmarian deglaciation mudrocks.	Lowermost Permian glacial diamictites (Tobra Formation) overlain by deglaciation shale (Dandot Formation)
Pre-Rift	Angular unconformity between the underlying Upper Devonian to Tournaisian limestones and the overlying syn-rift sequence Cambrian-Devonian succession	Ordovician-Carboniferous unconformity Gentle angular unconformity between Baghawala Formation (Cambrian) and Tobra Formation (Permo-Carboniferous) Salt Range Formation (Precambrian), Jhelum Group (Cambrian)

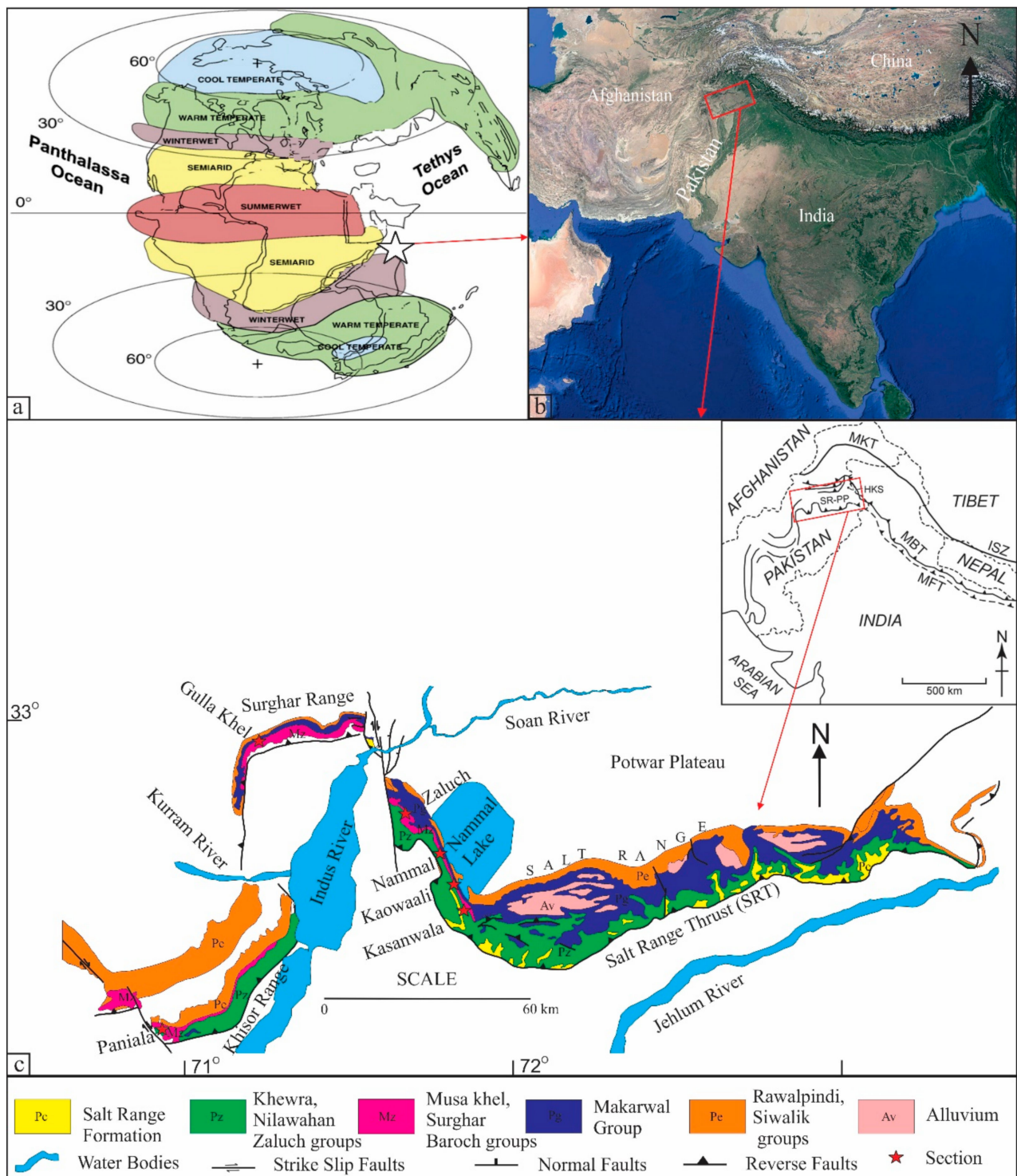


**Figure 1.** Current and palaeogeographic locations of the Salt Range, Pakistan. (a) Early Jurassic palaeogeographic location of the study area. The star marks location of the study area. (b) Google Earth view of Pakistan in regional context. The rectangle marks the location of Salt Range–Kohat–Potwar Plateau. (c) Salt and Trans–Indus ranges with locations of the studied sections. The inset map shows location of the Salt Range–Potwar Plateau (SR–PP) within the Himalayan orogenic belt. ISZ = Indus Suture Zone, MKT = Main Karakoram Thrust, HKS = Hazara–Kashmir Syntaxis, MBT = Main Boundary Thrust, MFT = Main Frontal Thrust (modified after [34–36]).

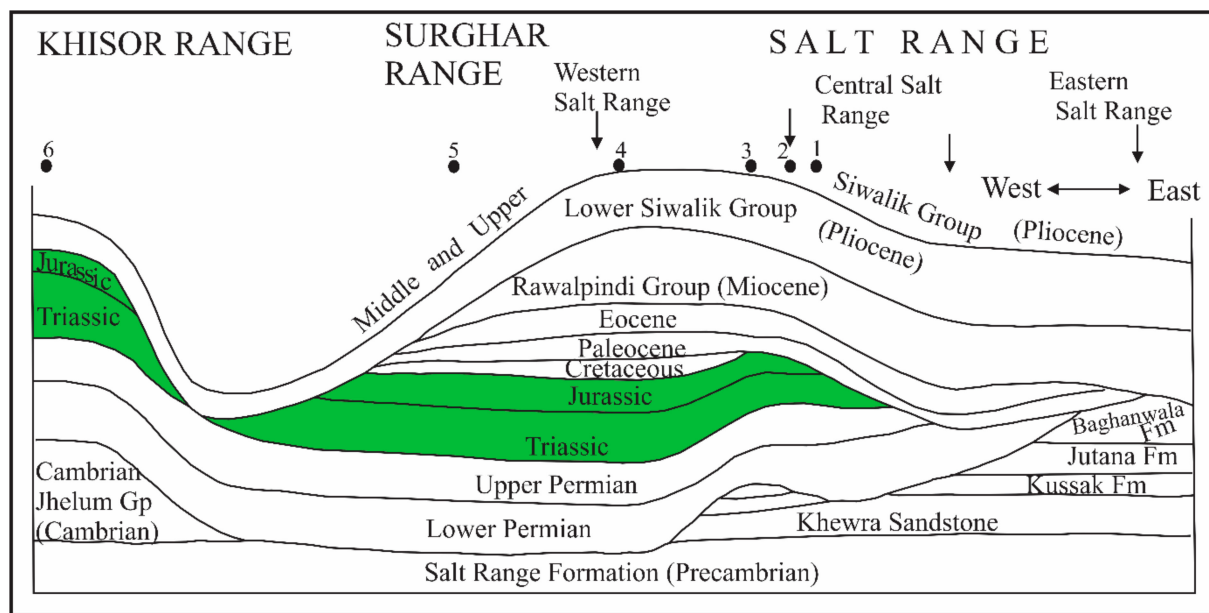


**Figure 2.** Generalised cross section of the Salt and Trans-Indus ranges showing the distribution of lithostratigraphic units in different parts of the area. Note the angular unconformity between the Cambrian and Permian strata and the absence of Mesozoic strata in the eastern Salt Range. The studied strata are highlighted in green colour. The studied sections are numbered 1–6. 1 = Kasanwala; 2 = Kaowali; 3 = Nammal Gorge; 4 = Zaluch Nala; 5 = Gulla Khel; and 6 = Paniala. Lower Permian (Tobra, Dandot, Warchha, and Sardhai formations), Upper Permian (Amb, Wargal, and Chiddru formations), Triassic (Mianwali, Tredian, and Kingriali formations), Jurassic (Datta, Shinawari, and Samana Suk formations), Cretaceous (Chichali, Lumshiwai, and Kawagarh formations), Paleocene (Hangu, Lockhart, and Patala formations), Eocene (Nammal, Sakesar, and Chorgali formations), Miocene (Murree and Kamliyal formations), and Plio-Pleistocene (Chinji, Nagri, Dhok Pattan, and Soan formations) (modified from [37]).

## 2. Geological Setting and Palaeogeography

The Salt Range, with its Trans Indus extension, is a nearly east–west trending mountain range located in Pakistan (Figure 1). The SRS preserves thick Precambrian to recent sedimentary record e.g., [36,37,40,46–48]. According to the literature, the SRS displays considerable similarity to the THS e.g., [16,19,23]. The SRS can be broadly subdivided into four supersequences similar to that of the THS (Table 1): (a) the Late Neoproterozoic–Cambrian sequence consists of evaporites of the Salt Range Formation and overlying siliciclastics of the Cambrian Jhelum Group that can be correlated with the pre-rift sequence of the THS; (b) the Lower Permian siliciclastics of the Tobra and Dandot formations of the Nilawahan Group, which are correlatable with the syn-rift sequence of the THS; (c) the middle Permian–Cretaceous sequence, which can be correlated with the drift sequence of the THS; and (d) the Paleocene–Eocene sequence, a probable stratigraphic equivalent of the syncollisional sequence of the THS. This succession of the SRS is capped by postcollisional siliciclastics of post Eocene age.

The SRS displays a major Ordovician–Carboniferous unconformity between the pre-rift and the syn-rift supersequences (Figure 2 and Table 1). This points towards the possible occurrence of the Cambro-Ordovician orogeny in the Salt Range that is documented over large parts of Gondwana [49,50]. The Ordovician to Carboniferous strata is, however, well developed in the Peshawar Basin [38] located ca. 200 km to the north of the Salt Range.

The syn-rift sequence on the northwestern margin of the Indian Plate documents the tectonic processes that resulted in the continental break-up and Neo-Tethys opening. The drift sequence of the area preserves the sedimentation and subsidence history of the NW passive continental margin of the Indian Plate [51–53]. The sudden increase in siliclastic detritus during the Late Triassic points to a possible passive-margin rejuvenation in the NW Greater India. Quartzose sandstones were deposited during this interval in THS



and this deposition locally continued until the middle Early Jurassic [16]. The quartzose sandstones of the SRS around the TJB interval were possibly deposited during this passive margin rejuvenation phase. The Kingriali Formation consists of dolostones, limestones with green-black shales, and sandstones in the upper part. A Rhaetian age is confirmed by new palynology data [15]. The Datta Formation, of Hettangian age, consists of conglomerates, sandstones, shales, and carbonates.

Around 200 Ma ago, the Salt Range (Figure 1) was located on the NW margin of the Indian Plate, close to the Arabian and Greater Somalian plates, in the tropical-near tropical region of the southern hemisphere in the Tethyan realm at  $\sim 20^{\circ}$ – $25^{\circ}$  S latitude [34,54,55]. The TJB interval witnessed a transition from hot and arid to hot and humid greenhouse palaeoclimate [56–58]. During this interval, a fluvio-deltaic system developed in the areas, nowadays the Salt Range–Kohat–Potwar Plateau, and deposited the siliciclastics of Kingriali and Datta formations on an area of ca. 15,000 km<sup>2</sup> [15,36].

### 3. Material and Methods

#### 3.1. Fieldwork and Sampling

In the Salt and Trans Indus ranges of Pakistan the upper part of the Kingriali Formation and the overlying entire Datta Formation were studied (Figure 1b,c). A total of six (6) stratigraphic sections were measured along a ca. 300 km transect from the western Salt Range through the Surghar Range, and the Khisor Range (Figures 2 and 3; Table 2).

Sedimentological analyses were conducted in the field (Figures 2–5). In total, 400 samples were collected from the entire facies' variation.

#### 3.2. Palaeocurrent Analysis

Palaeocurrent data, mostly from trough cross bedding and where possible from the imbricated clasts and ripples, were collected. In total, 229 readings for palaeocurrents were collected in the field, including 209 from cross bedding and 20 from imbricated clasts and ripples. For each reading, measurements of the dip and azimuth of the structure and dip and strike of the beds were taken using a Brunton compass. The direction for each reading was recorded as a plunge with respect to the orientation of the bedding, and this direction was then rotated back to the depositional horizontal using stereonet techniques [59]. The data were restored to reconstruct the palaeoflow pathway and rose diagrams were prepared for each stratigraphic section (Figure 5).

**Table 2.** Geographic positions of the studied sections in the Salt and Trans Indus ranges.

S. No	Locality Name	Area	Latitude	Longitude
1	Kasanwala Nala	Salt Range	32°36/14.17//N	71°49/45.63//E
2	Kaowaali		32°37/1.28//N	71°49/13.00//E
3	Nammal Gorge		32°39/43.83//N	71°47/48.23//E
4	Zaluch Nala		32°46/1.45//N	71°39/54.06//E
5	Gulla Khel	Surghar Range	32°58/28.80//N	71°13/23.17//E
6	Paniala	Khisor Range	32°13/25.19//N	70°53/49.33//E

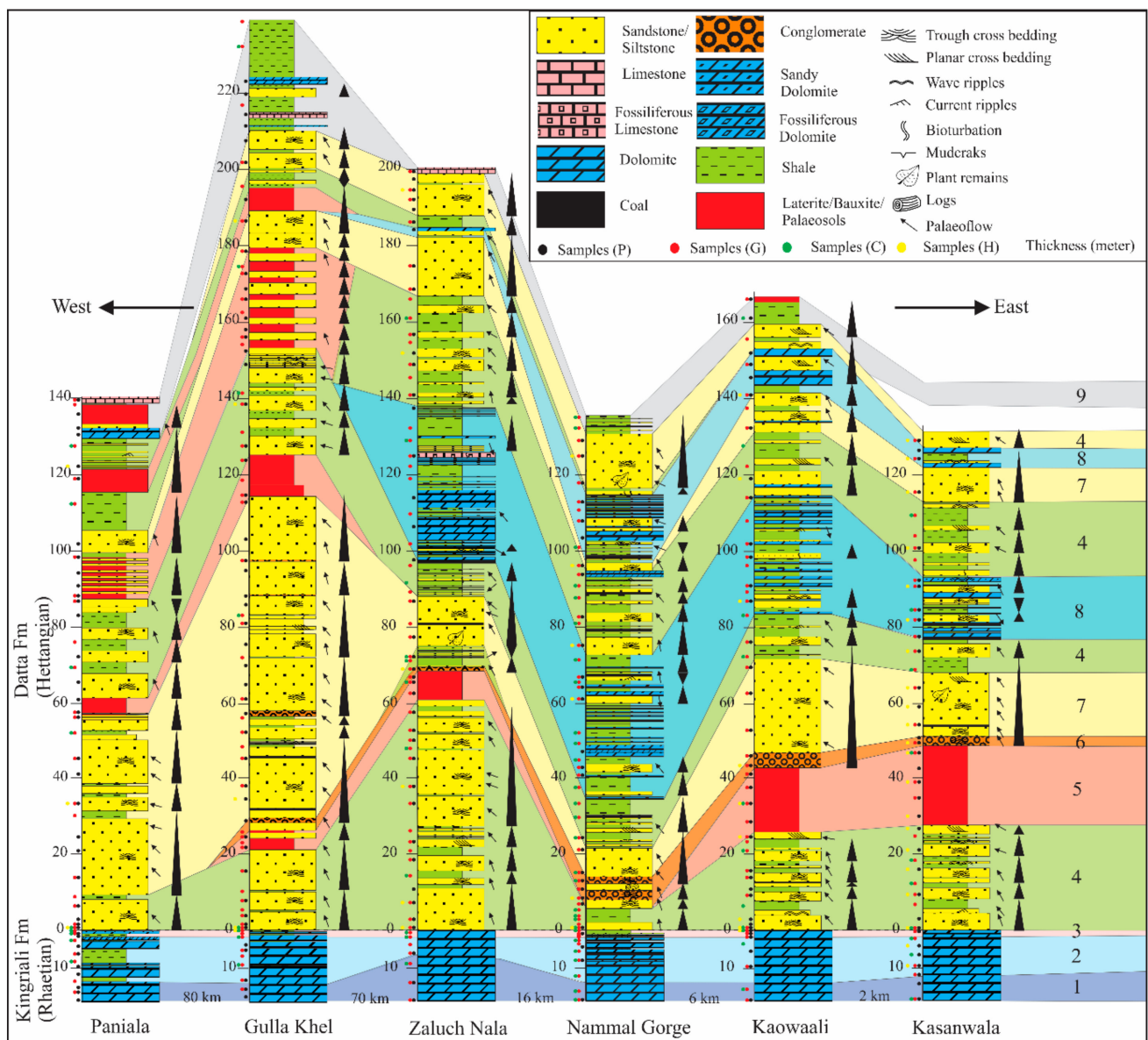


**Figure 3.** Measured stratigraphic sections in the Salt and Trans-Indus ranges. Sedimentary structures, sample locations, and grain size trend are displayed on each log. Vertical facies variation is displayed and a general lithofacies correlation is also marked on the lithological logs. 1 = dolostone lithofacies; 2 = shallow marine dolostone and shale lithofacies; 3 = lagoonal shale and evaporites lithofacies; 4 = channel margin sandstone lithofacies and overbank-floodplain shale lithofacies; 5 = laterite-bauxite lithofacies; 6 = channel belt conglomerate lithofacies; 7 = channel belt sandstone lithofacies; 8 = lagoonal shale lithofacies and lagoonal carbonates lithofacies; and 9 = contact zone with the overlying strata. The distance between each section is displayed in kilometers. (P) = petrography; (G) = geochemistry; (C) = clay mineralogy; (H) = heavy minerals.



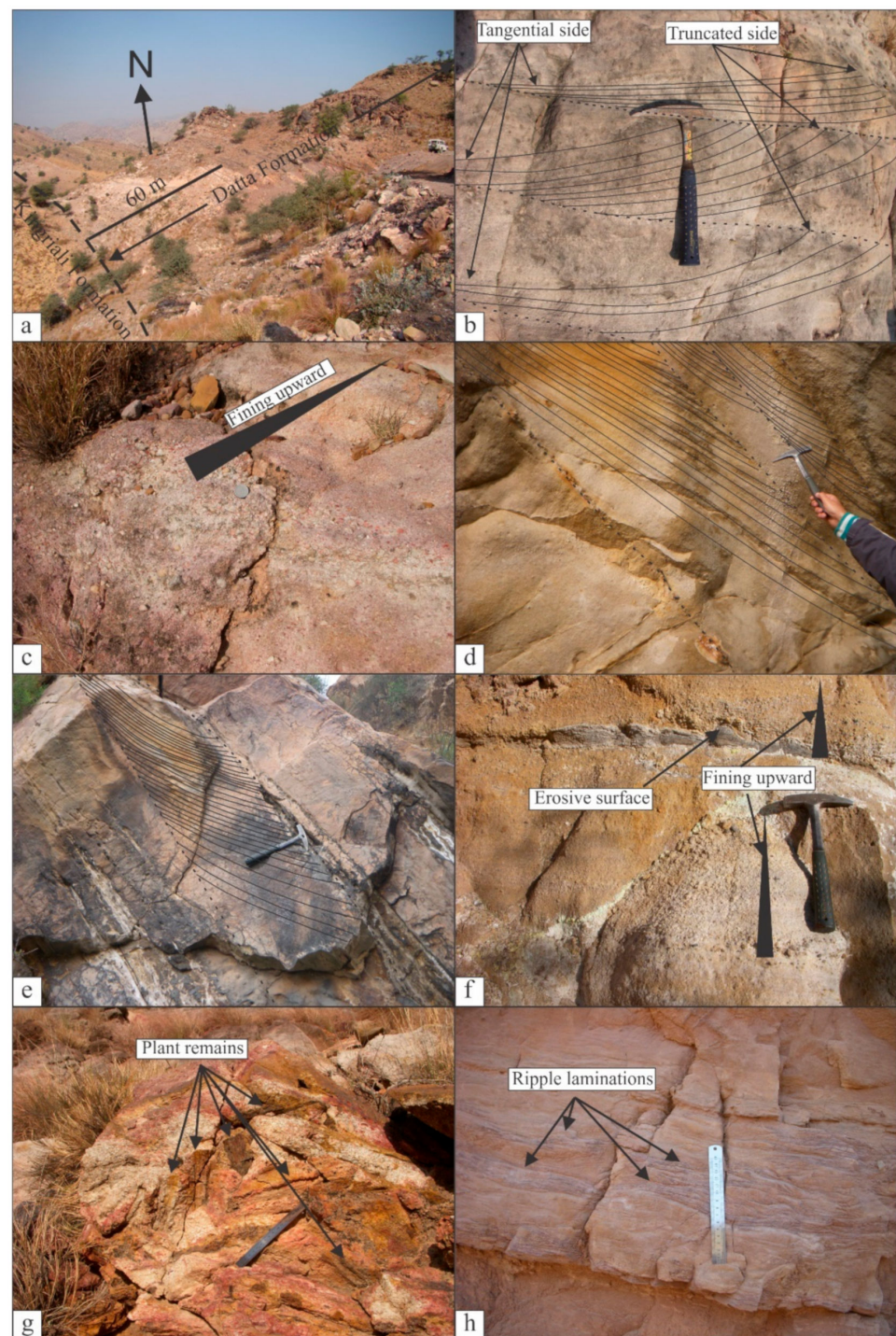


**Figure 4.** Representative field photographs showing: (a) an overview of the upper part of the Kingriali Formation and the Datta Formation in Zaluch Nala; (b,d,e) cross bedding (dominantly trough cross bedding) with the tangential and truncated side labeled in the Datta Formation at Kasanwala, Kaowaali, and Nammal Gorge, respectively; (c) quartz-rich conglomerate in the Datta Formation at the Kasanwala section; (f) laminated siltstone with erosive upper bedding plane and fining upward quartz rich pebbly sandstone in the Datta Formation at Nammal Gorge; (g) plant remains in pebbly sandstones of the Datta Formation at Kasanwala; and (h) ripple-laminated fine grained sandstone in the Datta Formation at Gulla Khel.

### 3.3. Petrographic Studies

Except for loose shale, thin sections were made for all siltstones, sandstones, conglomerates, carbonates, and evaporites samples. In total, 300 thin sections were made at the Department of Geology, University of Vienna. All thin sections were studied systematically using a Leica DM2700 P microscope with a Leica MC170 HD camera. Herein, the petrographic studies were focused on point counting of 500 grains per thin section (Supplementary Materials S1) and its application for provenance analysis. The petrographic detail of the carbonates present in the succession are avoided as these are not significant in provenance analysis. Similarly, the various types of cementation and diagenetic features add little to the provenance analysis and have been avoided.

For point counting, the total quartz ( $Q_{total}$ ) was subdivided into monocrystalline ( $Q_m$ ) and polycrystalline ( $Q_p$ ) varieties. The latter also included chert.  $Q_m$  was further classified into  $Q_m$  with unit extinction ( $Q_{mue}$ ) and  $Q_m$  with undulose extinction ( $Q_{muu}$ ). Similarly,  $Q_p$  was subdivided into  $Q_p$  with 2–3 crystals ( $Q_{pq(2-3)}$ ) and  $Q_p$  with >3 crystals ( $Q_{pq>3}$ ). Total feldspars ( $F_{total}$ ) were subdivided into plagioclase (P) and K-feldspar (A). The total lithic fragments ( $L_{total}$ ) were subdivided into sedimentary ( $L_s$ ), metamorphic ( $L_m$ ), and volcanic-metavolcanic ( $L_v$ ) lithics [60,61]. The data were plotted on Quartz–Feldspars–Lithic fragments (QFL) plots for sandstone classifications and tectonic setting discrimination [62].

### 3.4. Clay Mineralogy/XRD Separation

Thirty samples from the clays/shale horizons were selected and investigated for clay mineralogy. These include 10 samples from the Kingriali Formation and 20 samples from the Datta Formation. XRD separation analysis was conducted using a PANalytical X'Pert Pro diffractometer (CuK $\alpha$ -radiation (40 kV, 40 mA), step size 0.0167, 5 s per step) at the University of Vienna. Each sample was treated with 15% hydrogenperoxide (H<sub>2</sub>O<sub>2</sub>) to remove the organic matter [63] and then dispersed with a 400 W ultrasonic probe. The <2  $\mu$ m fraction of each sample was separated using Atterberg cylinders and dried in oven at a temperature <40 °C to avoid the destruction of kaolinite. Then, 1 mL suspension (10 mg/mL) of each sample was pipetted out onto a glass slide to prepare oriented clay samples. Each sample was saturated with Mg and K ions and the mounts were analysed. These samples were saturated with glycerol (Mg-samples) and ethylene-glycol (K-samples) to separate smectite and vermiculite. Every sample was heated to 550 °C [64] and analysed as kaolinite loses its structure at this temperature. The XRD patterns were interpreted [65] and quantified using the correction factors [66].

### 3.5. Bulk Geochemistry

In total, 150 samples were selected, including 40 samples from the Kingriali Formation and 110 samples from the Datta Formation, for bulk rock geochemical analysis based on field and petrographic studies. Each sample was powdered and homogenised and the analysis was conducted at Bureau Veritas, Canada using inductively coupled plasma optical emission spectroscopy/mass spectrometry (ICP-OES/MS). The analysis included major, minor oxides, trace, and rare earth elements (REEs) (Supplementary Materials S2).

For each sample, a split of 0.2 mg powdered and homogenised sample was fused in lithium metaborate/tetraborate followed by nitric acid digestion to extract Si, Nb, and Rb and measured by ICP-OES (Spectro Ciros Vision). Besides, 0.5 g of each sample was digested in 95 °C Aqua Regia and analysed for Al, Fe, Mg, Ca, Na, K, Ti, P, Mn, Cr, Ba, Co, Sr, Th, U, V, W, and Zr using ICP-MS (Perkin Elmer ELAN 9000, Sciex). Both splits were calibrated against reference materials SO18, DS 10, and OREAS 45 EA. Thirteen samples were analysed in duplicates. The average analytical error in the analysis is 0.18%.

The interpretation of geochemical data is based on widely used proxies to reconstruct weathering and palaeoclimatic trends including the Chemical Index of Alteration (CIA) [67,68], Al<sub>2</sub>O<sub>3</sub>–CaO\*+Na<sub>2</sub>O–K<sub>2</sub>O (A–CN–K) plot, and Th/U versus Th plot [69]. In both the CIA and A–CN–K, all the quantities were used in molar proportions and the CaO\*



is the amount of CaO incorporated in the silicate fraction of the rock and correction for K-metasomatism was also made [70]. Th/Sc versus Zr/Sc plot [71] was used to understand the sediment recycling. Th/Co versus La/Sc plot [72] and V-Ni-Thx10 plot [73] were used for the identification of parent rocks composition. La/Th versus Hf plot [74]; Ti/Zr versus La/Sc, La-Th-Sc, Th-Sc-Zr/10, and Th-Co-Zr/10 plots [75]; and Nb/La versus (La/Sm)N plot have been used for discrimination of tectonic settings. These proxies are widely used for provenance analysis worldwide e.g., [76–87].

### 3.6. Heavy Minerals

Subsequent to detail petrography and geochemistry, 30 rock samples from the siltstones and sandstones of the succession (Supplementary Materials S3) were selected for heavy mineral analysis. Each sample was gently crushed to separate the constituent particles. A solution of 3:2 distilled water and 80% acetic acid was prepared to decalcify each sample. Each of the treated samples was sieved to separate the 0.4 mm to 63  $\mu\text{m}$  fraction used for the heavy mineral separation e.g., [84]. Heavy minerals were separated by gravity settling in low-toxicity inorganic solutions, based on tungsten compounds lithium heteropolytungstates (LST) with a specific gravity of 2.90  $\text{g}/\text{cm}^3$  [88,89]. The grain concentrates containing the whole heavy mineral fraction were embedded in a Canada Balsam mount. Herein, heavy mineral data for the Kasanwala section are presented as this section preserves the complete lithofacies variations of the succession.

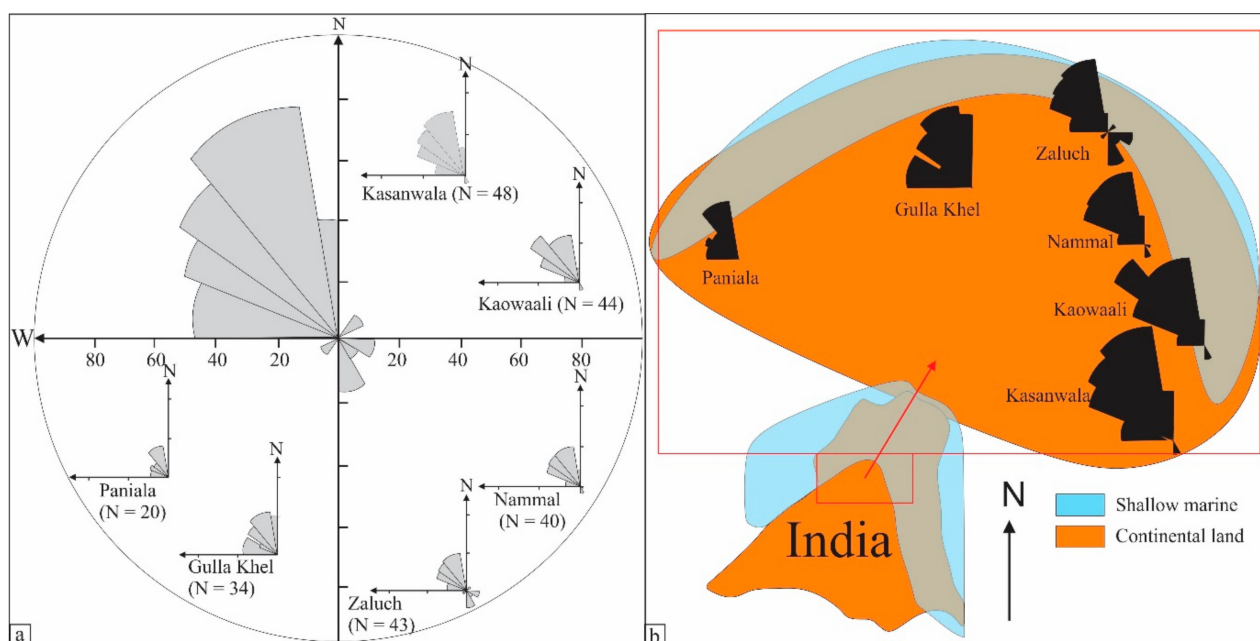


**Figure 5.** (a) Restored palaeoflow data from cross-strata favouring a north-northwestward palaeo-flow. The number of readings (N) is indicated for each section on the horizontal axis (total 229). Both the rotation of the Indian Plate and tilt of the strata are considered for the palaeoflow restoration. (b) Palaeoflow data plotted on the palaeogeographic map of the area (locations are tentative and not to the scale) [90].

## 4. Results

### 4.1. Field Data

A summary of the outcrop observations and facies distribution based on the present study is included in Table 3. Herein, information just relevant in the provenance analysis is included. The Kingriali Formation consists mainly of thick-bedded dolostone displaying various shades of a gray colour. The formation forms distinct ridges of variable thickness from the western Salt Range (75 m–85 m) to the Surghar Range (92 m–108 m). Thin beds of

dark green, brownish-black shales and sandstones occur in the upper part of the formation, indicating the onset of siliciclastic supply to the basin (Figure 3).

**Table 3.** Lithofacies and lithofacies associations observed in the Kingriali and Datta formations during the present study. The lithofacies classification is based on their depositional setting. Only the first occurrence in a complete cycle is presented and the lateral distribution in the Salt and Trans–Indus ranges is included in the table.

Formation /Age	Lithofacies/ Environments	Lithology/Features	Lithofacies Association	Distribution		
				Salt Range	Surghar Range	Khisor Range
Datta Formation Jurassic (Hettangian)	Lagoonal carbonate	Yellowish orange to brown dolomites, ripple marks,	Lagoonal lithofacies Association	Present	Present only in eastern parts	Absent
	Lagoonal shale	Gray, calcareous shales, with siltstone, fine sandstone interbeds having ripples		Present	Present only in eastern parts	Absent
	Channel belt sandstone	Quartz rich sandstones, cross bedding, fining upward, coal patches and carbonaceous horizons, fining upward	Channel belt facies association	Present	Present	Present
	Channel belt conglomerate	Quartz rich conglomerates, cross bedding, flat pebbles imbrications, erosive bases, fining upward		Present	Absent	Absent
	Laterite–bauxite	Red-purple laterite–bauxite with kaolinite	Channel margin and overbank floodplain lithofacies association	Present	Present	Present
	Overbank-floodplain shale	Red, gray shales with fire clay deposits		Present	Present	Present
	Channel margin sandstone	Brown-red, fine–medium grained, quartzose sandstone interbedded with red, brown shale, ripples, graded bedding		Present	Present	Present
Kingriali Formation Triassic (Rhaetian)	Lagoonal shale and evaporites	Greenish gray shale with gypsum on top, illite rich	Lagoonal and shallow marine lithofacies association	Present	Present	Present
	Shallow marine dolomite and shale	Thin–medium bedded dolomite and interbedded greenish gray shale (illite rich), shale thickness increases upward, lateritic oxidation on top of upper dolomite beds		Present	Present	Present
	Dolomite	Thick bedded, massive dolomite, laminations, occasional cross bedding, oolitic	Platform carbonates lithofacies association	Present	Present	Present

The lower part of the Datta Formation consists of rounded, well-sorted, and quartzose conglomerates, as well as pebbly and coarse quartz rich sandstones (Figure 4a–e). The coarsest pebbles (average diameter = 5–7 cm) occur in the Kasanwala section (Figure 4c); the Zaluch Nala section displays finer pebbles (average diameter = 2–3 cm). In the Surghar and Khisor ranges, conglomerates are not present. Upsection, red-brown colour fine to medium grained sandstones, siltstones, and light to dark brown shale occur throughout the study area. Brown-black calcareous shale and carbonates are limited to the western Salt Range and eastern parts of the Surghar Range.

The conglomerates, pebbly sandstones, sandstones, and siltstones possess abundant trough cross-beds and cross bed sets (Figure 4b,d,e). Laminated siltstone with erosive upper bedding plane and fining upward pebbly sandstones occur in the Datta Formation at Nammal Gorge (Figure 4f). In the Kasanwala section, plant remains occur in the pebbly sandstones of the Datta Formation (Figure 4g). In the Gulla Khel section, ripple-laminated fine-grained sandstones are common in the Datta Formation (Figure 4h). Additionally, aligned pebbles with their longer axes parallel to the bedding plane and pebble’s imbrication indicative of transport direction occur. All these palaeoflow indicators indicate a general southeast to northwest transport of the sediments (Figure 5).

#### 4.2. Framework Composition/Petrographic Studies

The Triassic sandstones are fine to medium grained and consist of poorly sorted angular to subrounded clasts (Figure 6a,b). Silica and iron oxide are the major cementing material, while carbonate cements are minor. The grains display a sharp margin with point and long linear contacts. Corroded grain margins and sutured contacts are rare (Figure 6a).

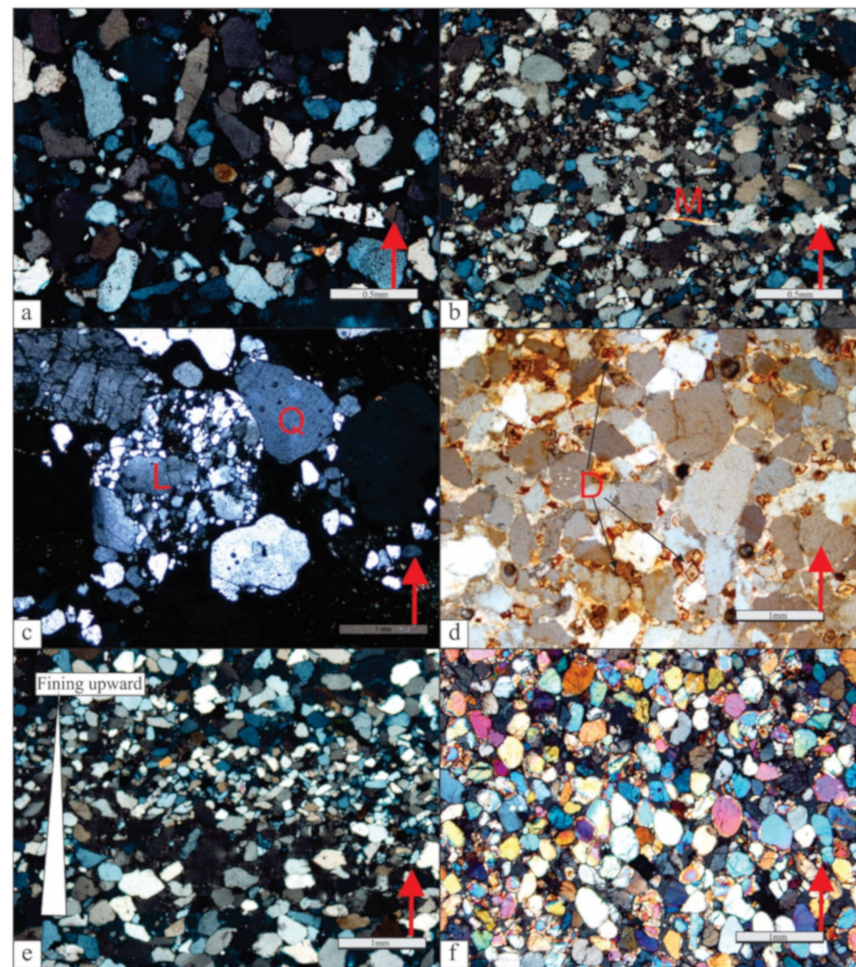


**Figure 6.** Representative thin section photomicrographs of the Kingriali and Datta formations siliciclastics. (a) Poor to moderately sorted, angular to subangular medium grained quartz rich sandstone with matrix and Fe-cement in the Kingriali Formation (Kasanwala); (b) subangular to subrounded poorly sorted fine grained sandstone of the Kingriali Formation (Kasanwala); (c) quartz-rich lithoclasts in well-rounded and very well sorted, pebbly sandstone of the Datta Formation (Nammal Gorge); (d) quartz-rich sandstone with carbonate cement and dolomite rhomb in the Datta Formation (Kasanwala); (e) fining upward cycle in quartz-rich sandstone at Gulla Khel; and (f) very well rounded and very well sorted quartz-rich sandstone in the Datta Formation (Nammal Gorge). Red arrow in each case indicates the top of bed. D = dolomite crystal; L = lithoclast; M = mica; Q = quartz.

The Jurassic sandstones are medium to very coarse grained and pebbly, are rounded to very well rounded, and are very well sorted (Figure 6c,d). A fining upward trend is observable in the sandstones (Figure 6e). Point and long linear contacts are common, and concavo-convex contacts are also observable, while suture contacts are rare (Figure 6f). Fine silt and clay size particles are present in the pore spaces of the coarse grained to pebbly sandstones. Iron oxide, calcite, dolomite/ferroan dolomite, and silica are the common cementing materials. Matrix is generally lacking, but where the grains are not in contact, they are floating in iron oxide, finely crystalline calcite, and dolomite (Figure 6c,d). Fractures filled with brown colour iron oxide are crosscut by sparry calcite veins/fractures.

Point counting data indicate that quartz is the dominant framework component and  $Q_{total}$  averages 98% in the Triassic strata (Figure 7a).  $L_t$  is 1%, while the sum of  $F_t$  and other framework components is 1%.  $Q_{total}$  is a mixture of  $Q_m$  (96%) and  $Q_p$  (4%).  $Q_m$  consists of  $Q_{mue}$  (90%) and  $Q_{muu}$  (6%), while  $Q_p$  consists of  $Q_{pq(2-3)}$  (3%) and  $Q_{pq>3}$  (1%) (Figure 7b).



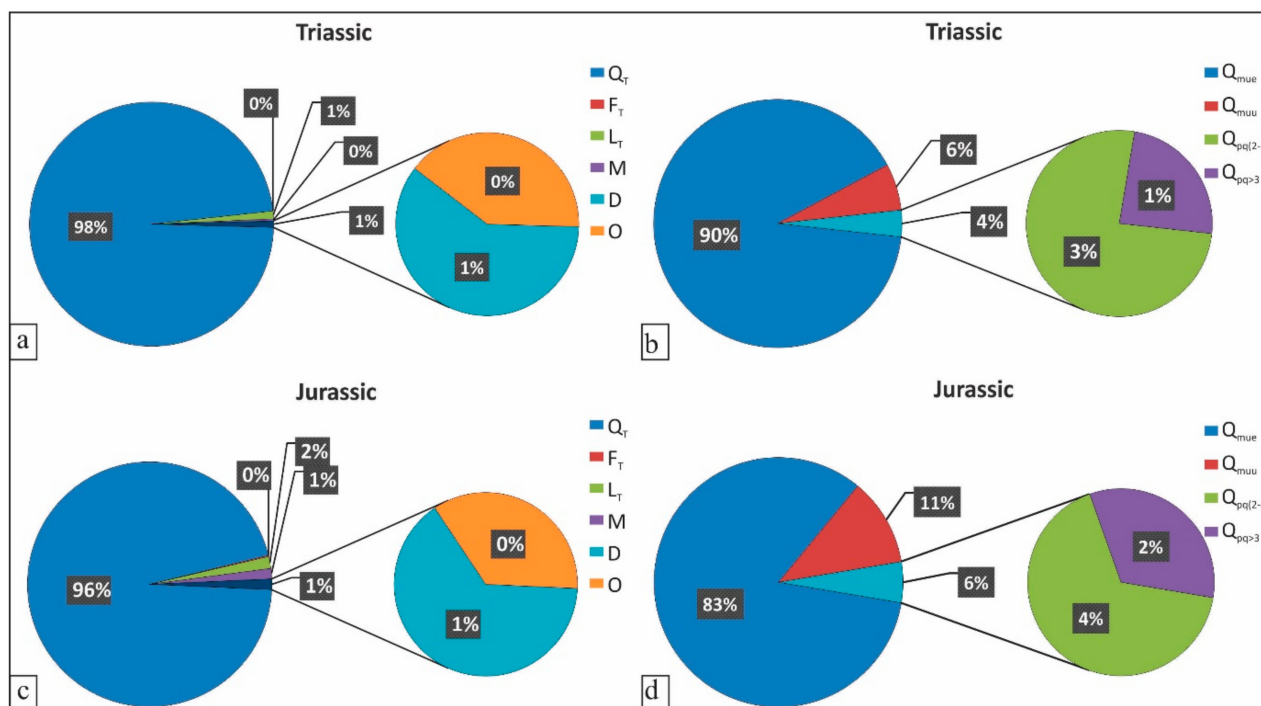


**Figure 7.** Framework mineralogical composition plots for the siliciclastics of the Kingriali and Datta formations. (a,b) Pie charts of the point count analysis showing quartz as the dominant framework composition in the Triassic strata; (c,d) pie charts of point count analysis showing quartz as the dominant constituent in the Jurassic strata and monocrystalline quartz has more undulose constituent.

The Jurassic strata consist of 96% average  $Q_{total}$  (Figure 7c).  $L_t$  averages 2% of the total framework composition, while  $F_t$  is less than 1% (Figure 7c). The  $Q_{total}$  consists of 94%  $Q_m$ , of which 81% is  $Q_{mue}$  and 11%  $Q_{muu}$ .  $Q_p$  counts for 6% of  $Q_{total}$  and is subdivided into 4%  $Q_{pq(2-3)}$  and 2%  $Q_{pq>3}$  (Figure 7d).

The average of the total point counting data indicates that  $Q_{total}$  averaged 96% of the total framework composition.  $Q_{mue}$  predominates, averaging 81%, followed by  $Q_{muu}$  (10%), whereas  $Q_{pq(2-3)}$  averages 3% and  $Q_{pq>3}$  averages 2%. Comparatively high  $Q_{muu}$  and  $Q_p$  contents occur in the conglomerates and pebbly sandstones. The  $F_{total}$  accounts for only 0.13%, of which A averages 0.12%, while P is 0.01%. The  $L_t$  averages 1.4% and is the combination of  $L_s$ ,  $L_m$ , and  $L_v$ . According to the  $Q_tF_tL_t$  plot, >96% of the samples plot in the pure quartzose field (Figure 8a). Around 97% of the samples plot in the undissected part of the continental block provenance field (Figure 8b).

#### 4.3. Clay Mineralogy

Analysis of the oriented clay samples displays a mixture of illite and kaolinite (Figure 9). Illite is the dominant clay mineral in the Kingriali Formation that averages 94% of the total clay content, while the remaining 6% is kaolinite. By contrast, the overlying Datta Formation is rich in kaolinite, which averages 69% of the total clays, while the remaining 31% is all illite. Following the very high illite content during the Triassic (100% in the uppermost part of the Kingriali Formation), a jump to very high kaolinite content (92%) is observed in the basal part of the Datta Formation (Figure 9).

#### 4.4. Bulk Geochemical Proxies

##### 4.4.1. Tectonic Settings Discrimination Plots

La/Th versus Hf(ppm), Ti/Zr versus La/Sc, and Nb/La versus (La/Sm)N Plots

The La/Th versus Hf(ppm) plot (Figure 10a) displays uniform low La/Th values of <8 and a wide range for Hf (1–30 ppm). More than 85% of the samples have La/Th values



of <5, while 80% of the samples have Hf values above  $\geq 3$  ppm. Moreover, 65% of the samples plot in the passive margin source field, while the remaining fall into the acidic arc source and mixed felsic/basic source fields.

The present samples have Ti/Zr ratios of <35 and a broad La/Sc range of 1 to >14. Around 75% of samples from the Kingriali Formation occupy the andesitic arc source and active continental margin fields. While the Datta Formation show 50% samples population in these fields and the remaining 50% are positioned in the passive margin source field (Figure 10b).

The Nb/La versus (La/Sm)N plot indicates that all the samples have an Nb/La ratio of <1.4 (Figure 10c). Similarly, the (La/Sm)N values are >3 for most of the samples (>95%). More than 90% of the samples plot in the passive margin settings.

#### La–Th–Sc, Th–Sc–Zr/10, and Th–Co–Zr/10 Plots

The results of the La/Th and La/Sc have already been included in the previous section. The Th/Sc ratio shows an average of 1.6 for the Kingriali Formation that increases to 2.8 for the Datta Formation. On the La–Th–Sc plot (Figure 11a), around 60% of the samples from the Kingriali Formation plot in the continental island arc field and 25% in the active and passive margins combined field. Moreover, 40% of the samples from the Datta Formation occupy the continental island arc field and 40% plot in the combined active and passive margin field (Figure 11a).

The Kingriali Formation has an average Zr/Th ratio of 12.5 that increases to 20.3 in the Datta Formation (Figure 11b). Around 85% of the samples from the Kingriali Formation plot in the active continental margin and continental island arc fields. On the contrary, 68% of the samples from the Datta Formation fall into the passive margin field of the Th–Sc–Zr/10 plot (Figure 11b). This percentage increases to 82% in the Th–Co–Zr/10 plot (Figure 11c).

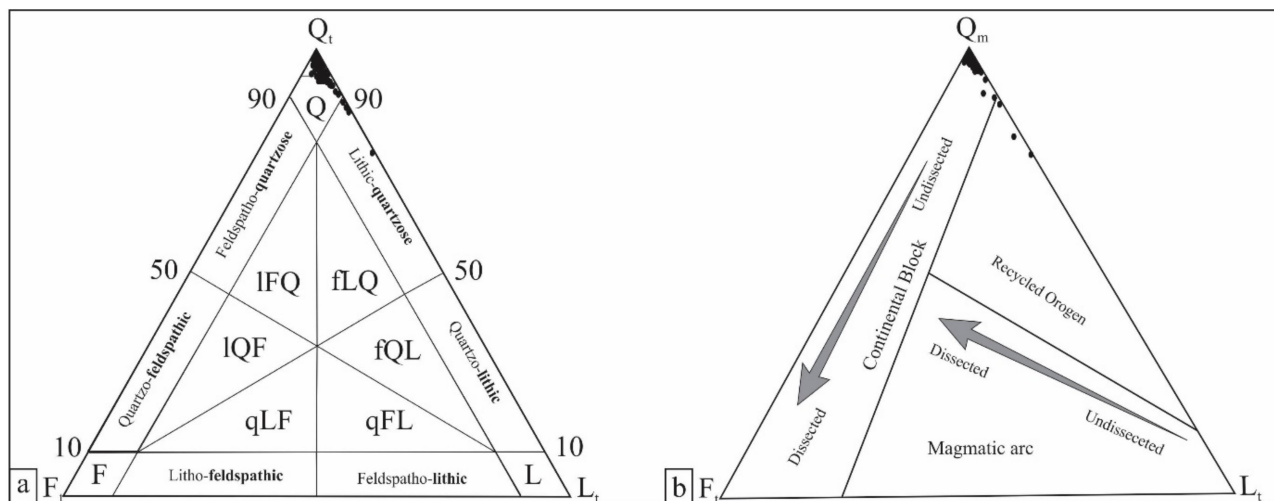


**Figure 8.** (a) Total Quartz–Feldspars–Lithics ( $Q_t F_t L_t$ ) plot for the sandstone’s classification [62], showing that majority of the sandstones are pure quartzose: Q = quartzose (qQ = pure quartzose); F = feldspathic; L = lithic; FQ = feldspatho-quartzose (ffQ = feldspar-rich; qFQ = quartz-rich); QF = quartzo-feldspathic; LF = litho-feldspathic; FL = feldspatho-lithic; QL = quartzolithic; LQ = litho-quartzose; IFQ = litho-feldspatho-quartzose; IQF = litho-quartzo-feldspathic; qLF = quartzo-lithofeldspathic; qFL = quartzo-feldspatho-lithic; fQL = feldspatho-quartzo-lithic; fLQ = feldspatho-litho-quartzose; (b)  $Q_m F_t L_t$  plot for tectonic setting discrimination [60], showing sediment derivation from undissected continental block.

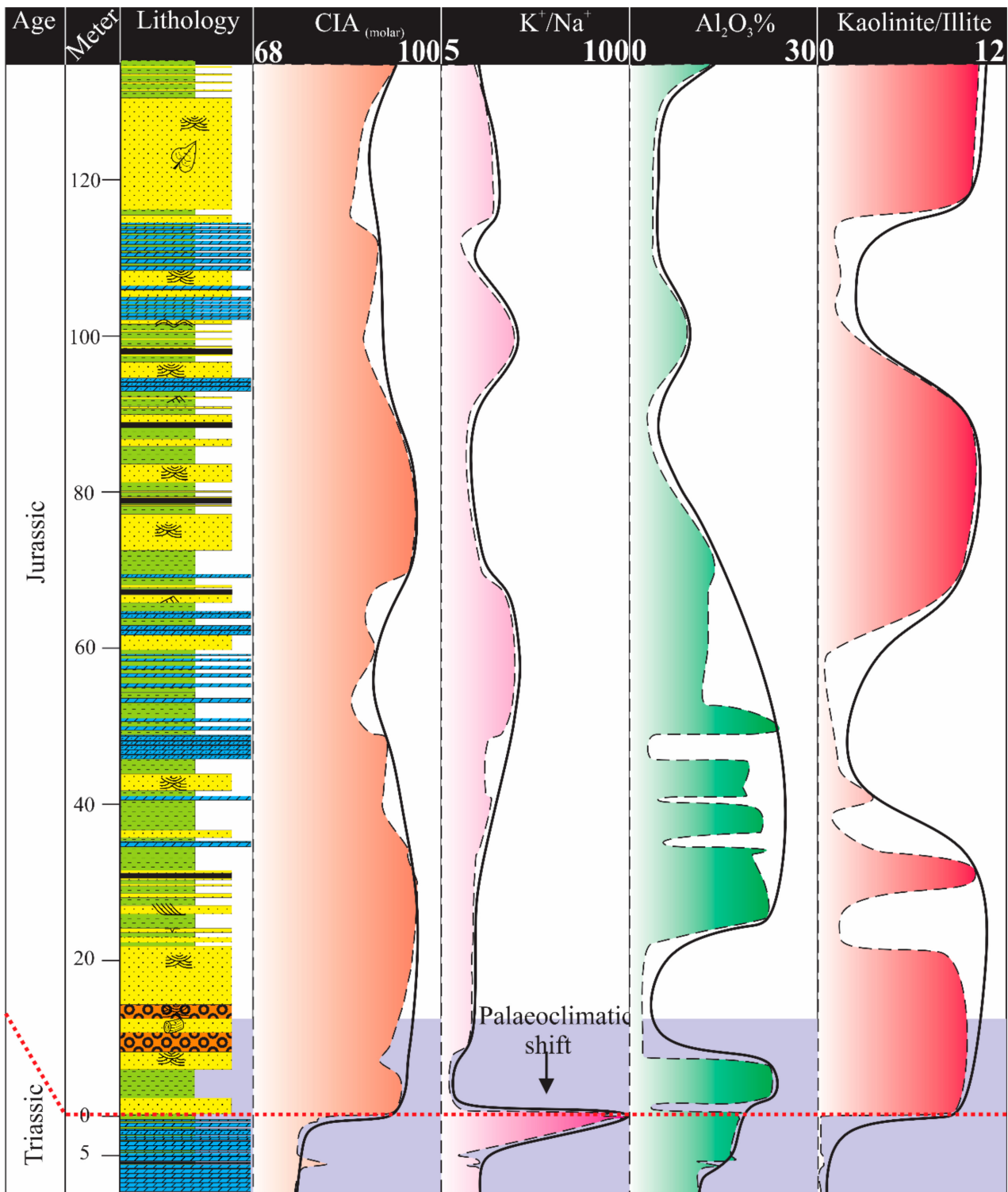


**Figure 9.** Lithological log of Nammal Gorge displaying vertical variation in Chemical Index of Alteration (CIA),  $K^+/Na^+$ ,  $Al_2O_3$ , and kaolinite/illite ratio. Note the sudden change in all the weathering proxies at the TJB interval. The Nammal Gorge section was selected to overcome the artifact in CIA and other proxies owing to laterites as this section lacks thick laterites.

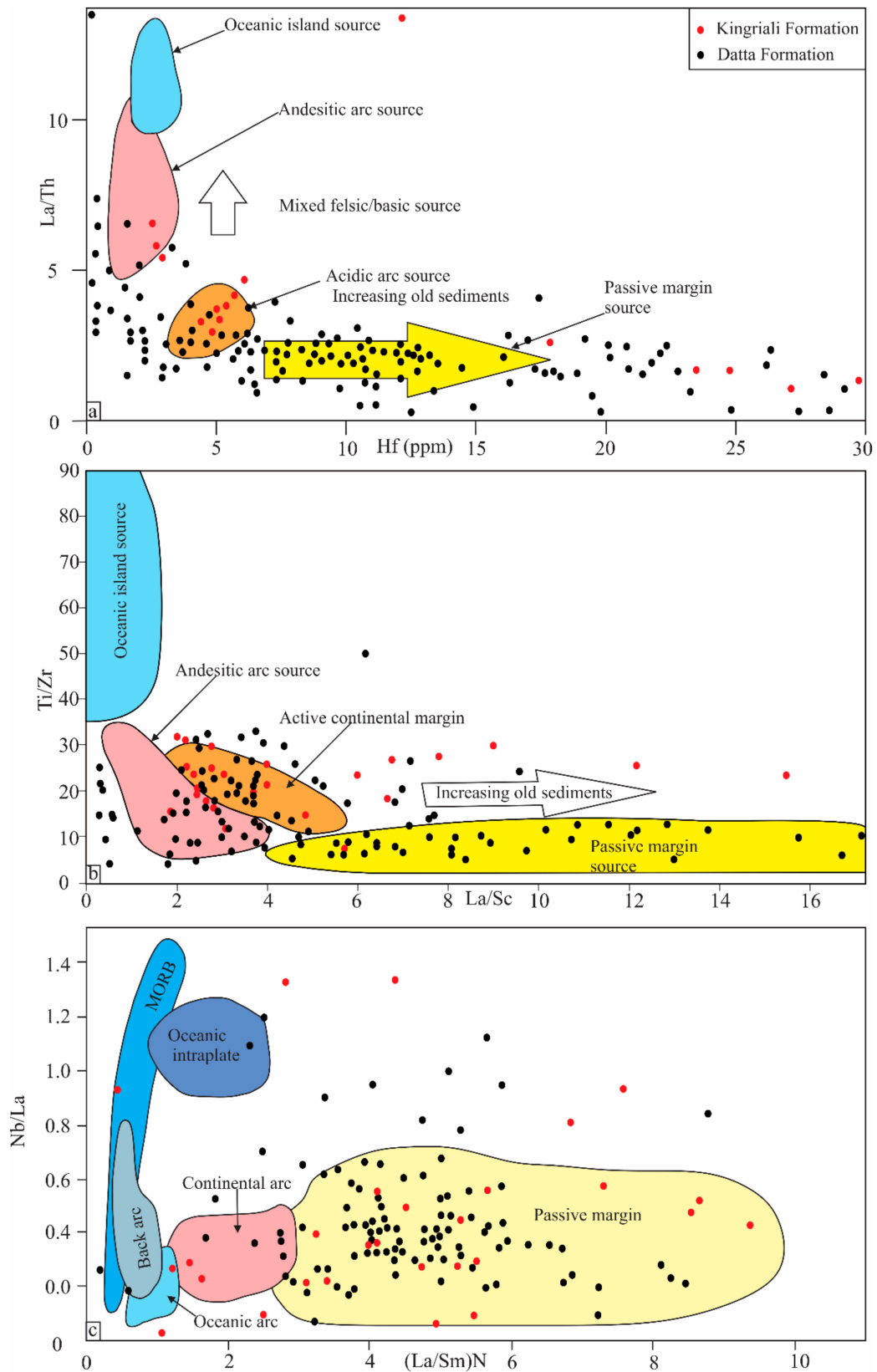


**Figure 10.** (a) La/Th versus Hf(ppm) bivariate plot [74], (b) Ti/Zr versus La/Sc bivariate plot [75] negating sediment derivation from oceanic island. Red dots are the Kingriali samples and black dots are the Datta samples in all figures, (c) Nb/La versus (La/Sm)N bivariate plot [91] indicating sedimentation on passive margin setting.

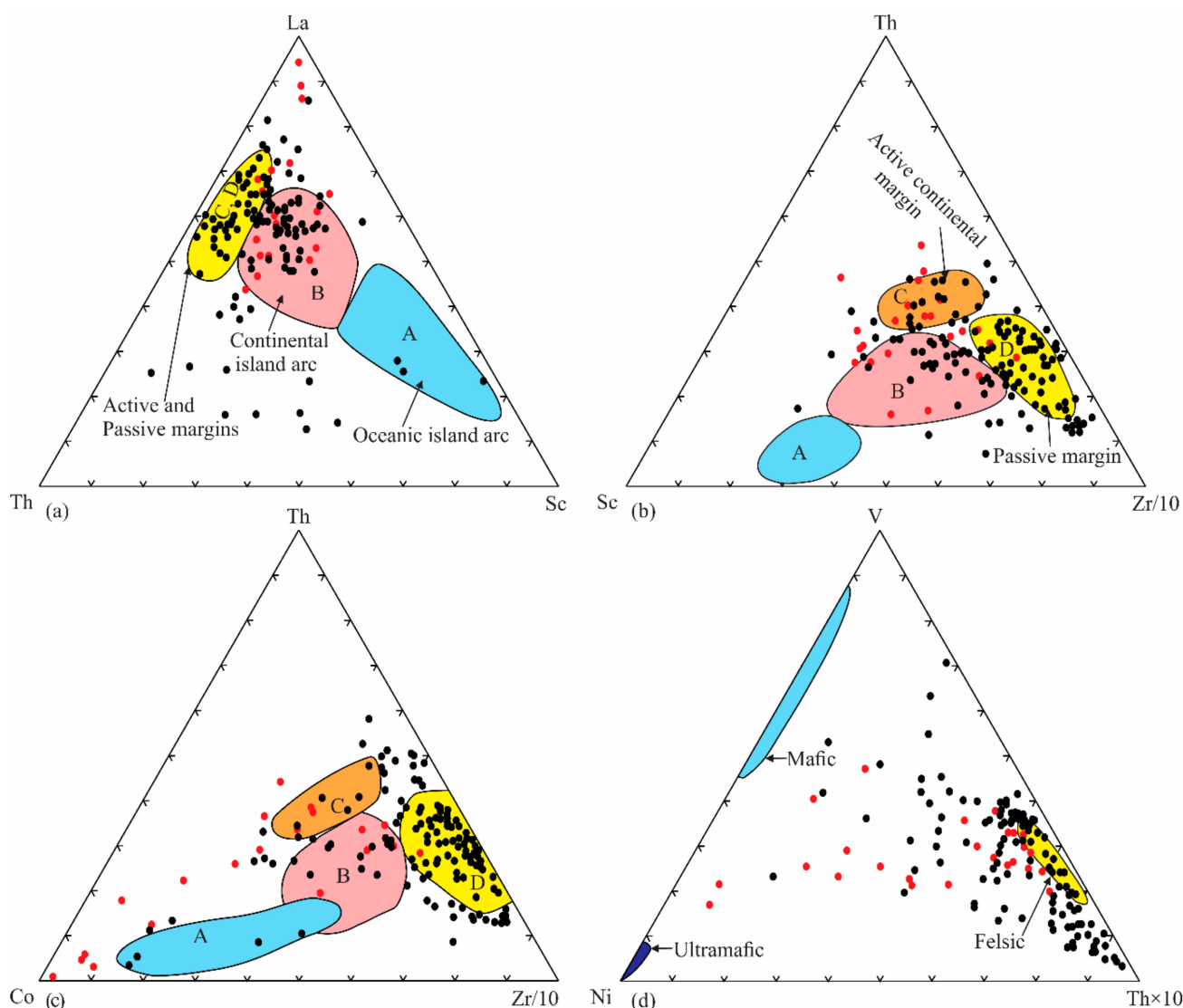


**Figure 11.** (a–c) La–Th–Sc, Th–Sc–Zr/10 and Th–Co–Zr/10 ternary plots [75] for tectonic setting discrimination indicating sediment derivation from the passive margin; (d) V–Ni–Th × 10 ternary plot [73] showing that the sediments were derived from a felsic source.

#### 4.4.2. Source Rock Composition Identification Plots

##### V–Ni–Th × 10 and Th/Co versus La/Sc Plots

The V–Ni–Th × 10 ternary plot indicates that all samples plot in the felsic source field or close to it (Figure 11d). By comparison, samples from the Datta Formation cluster more closely to the felsic field, while those of the Kingriali Formation are slightly off.

The Kingriali Formation displays La/Sc values of 2–10 and Th/Co values of 0.1–2. The Datta Formation has La/Sc values of 0.3–25 and Th/Co values of 0.4–17. The Th/Co versus La/Sc plot indicates a cluster of samples in the silicic rocks field (Figure 12a).

#### 4.4.3. Weathering and Recycling Trend

##### Chemical Index of Alteration (CIA) and A–CN–K Plot

The Kingriali Formation yielded low CIA values (Figure 9) ranging from 68.5 to 80 (average 77.7). By contrast, the Datta Formation yielded very high CIA values ranging from 88.8 to 99.8 (average 92.7). On the ternary plot A–CN–K, the present samples cluster near the A vertex roughly parallel to the A–K side (Figure 12d). Samples of the Kingriali



Formation plot in the muscovite–illite position and those of the Datta Formation are clustered close to the A vertex corresponding to the kaolinite position.

#### Th/U versus Th(ppm) and Th/Sc versus Zr/Sc Plots

The Th/U versus Th(ppm) plot indicates Th/U values below the upper continental crust (<3.8) for around 60% of the samples from the Kingriali Formation. In the Datta Formation (>90% samples), these values are above the upper continental crust (Figure 12b).

The Th/Sc versus Zr/Sc plot illustrates that >95% of the samples yield Th/Sc values above 1 (Figure 12c). Similarly, >95% of the samples show Zr/Sc values above 10. In general, the Datta Formation yielded higher Th/Sc and Zr/Sc values than the Kingriali Formation (Figure 12c).

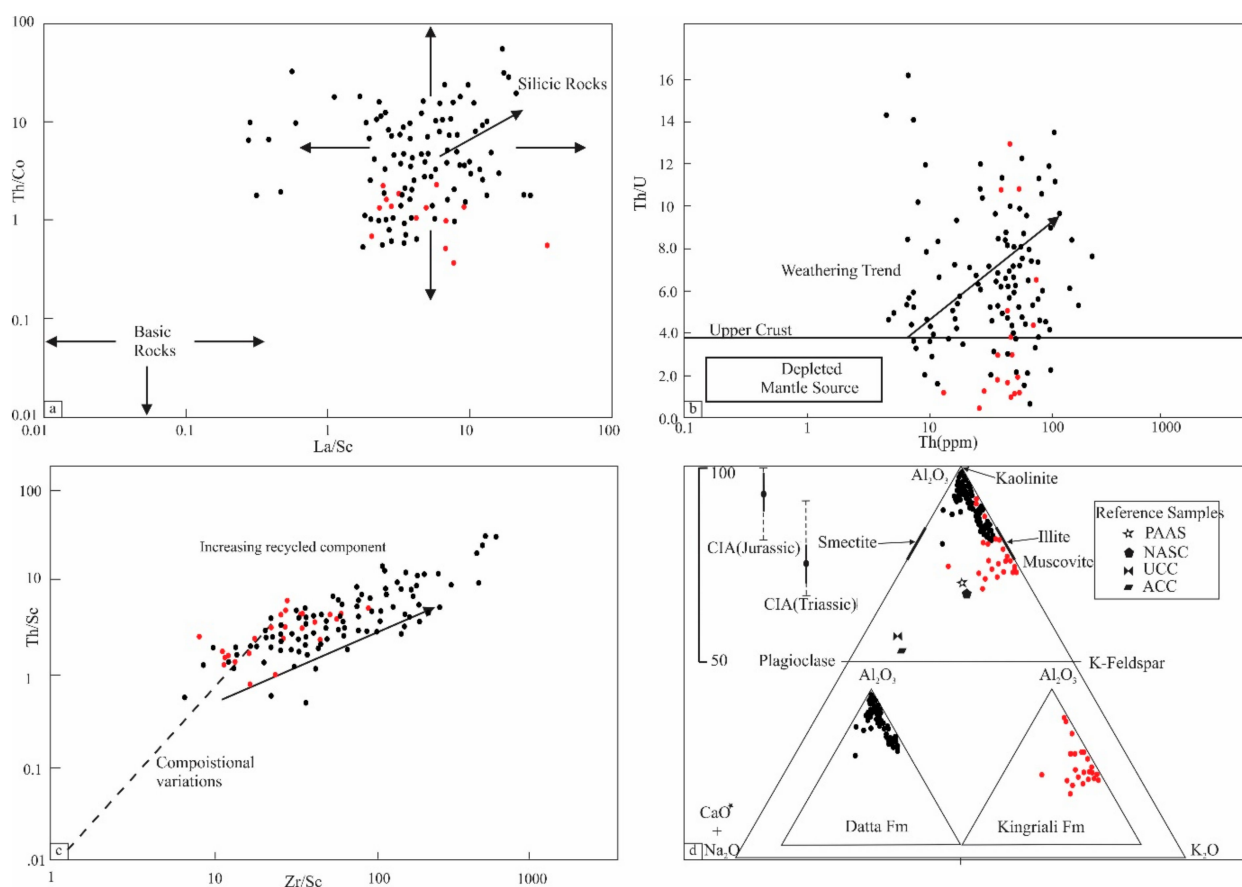


**Figure 12.** (a) Th/Co versus La/Sc plot [72] indicating sediment derivation from a silicic source; (b) Th/U versus Th(ppm) plot [69] favouring chemical weathering of the sediments; (c) Th/Sc versus Zr/Sc plot [71] supporting the recycled origin of the sediments; and (d) A–CN–K plot for the studied samples, where positions of reference minerals (muscovite, illite, smectite, and kaolinite) are indicated on the plot [92]. The Triassic and Jurassic samples are separated in the lower part of the plot and the CIA range (dotted and dashed lines) and average (black dots) are plotted to left for both the Triassic and Jurassic samples. PAAS = Post Archaean Australian Shale; NASC = North American Shale Composite; UCC = Upper Continental Crust; ACC = Average Continental Crust (ACC) [93–95].

#### 4.5. Heavy Minerals Analysis

In the present case, the heavy mineral assemblage represents a simple mixture (Supplementary Materials S3) of ultra-stable zircon, tourmaline, and rutile with minor staurolite and rare chloritoid. In general, the Triassic heavy minerals are smaller in size; have well preserved crystal faces, sharp edges, and corners; and display less dissolution and corrosion effects. The Jurassic heavy minerals are comparatively bigger in size and display advanced stage corrosion and dissolution and are rounded and broken (Figures 13 and 14).

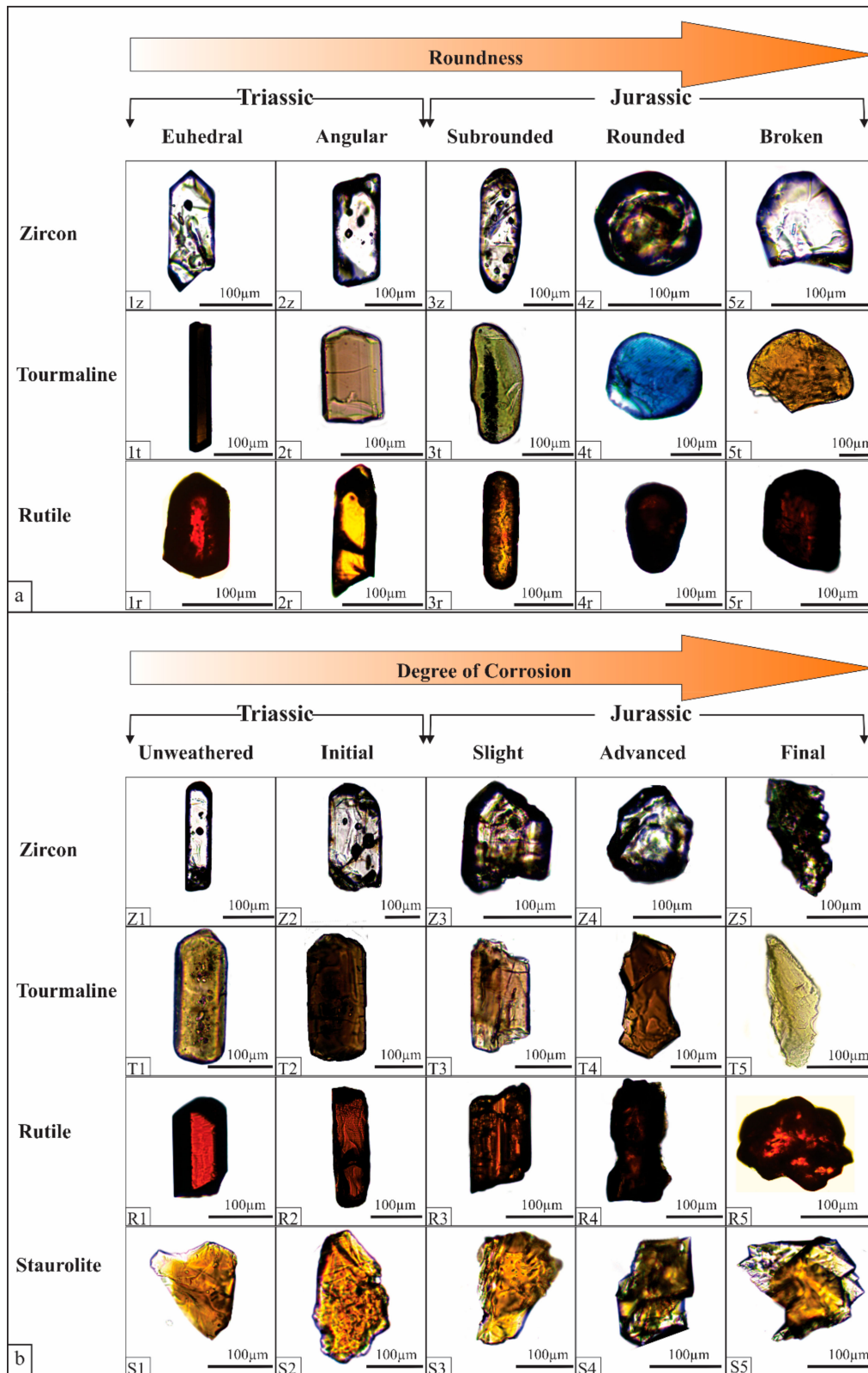


**Figure 13.** (a) Representative heavy minerals plotted in order of increasing degree of roundness from left (euhedral) in Triassic strata to right (broken) in Jurassic strata at Kasanwala, (b) representative heavy minerals indicating an increasing degree of corrosion from left (unweathered stage) in Triassic strata to right (extreme stage) in Jurassic strata at Kasanwala.

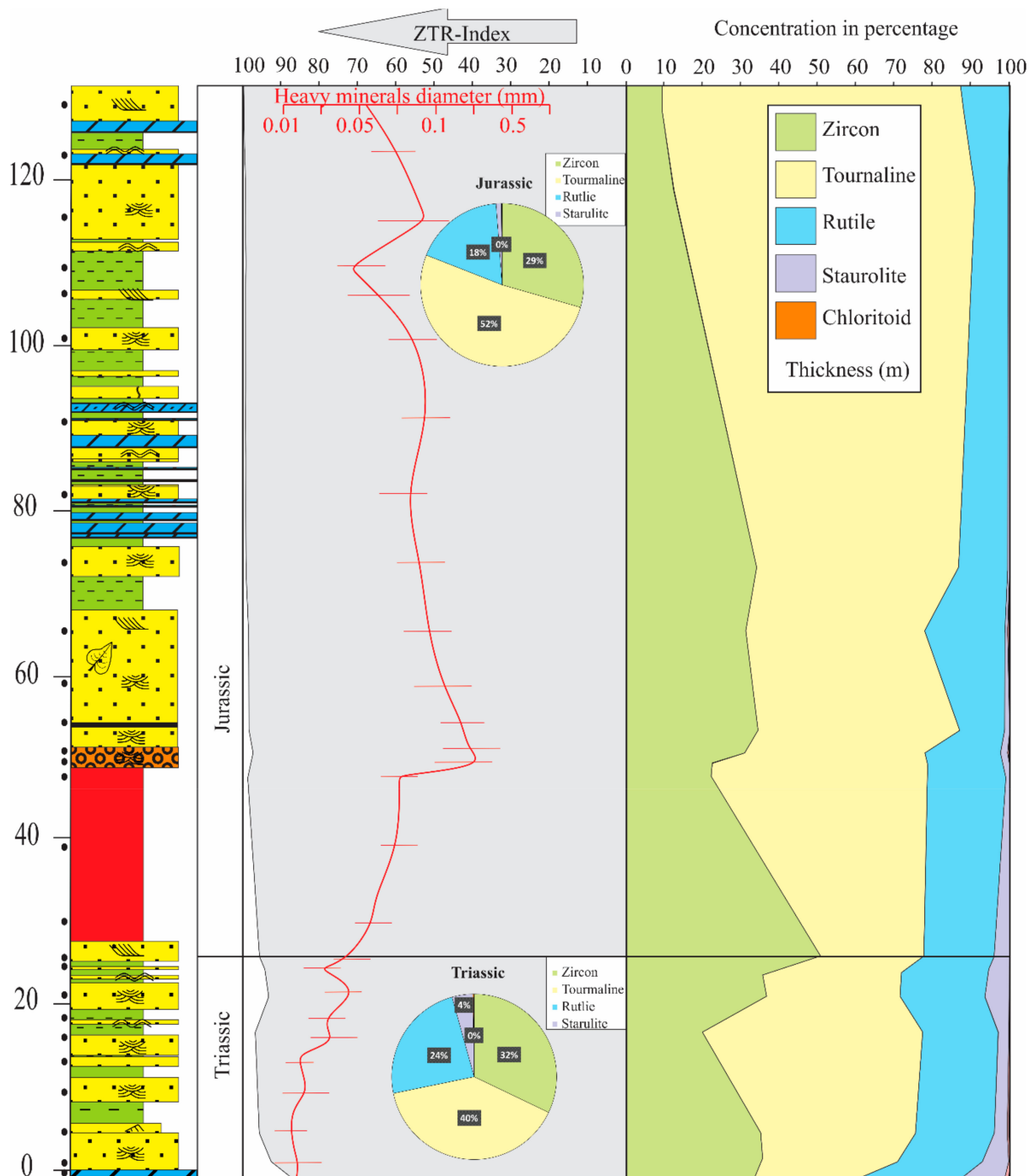


**Figure 14.** Heavy mineral's distribution in the Kasanwala section. ZTR-Index [96] is displayed to the left side, indicating an overall very high sediment maturity. A vertical grain size plot is included to have an idea of the grain size variation from Triassic to Jurassic. Pie charts of the point counting for heavy minerals for Triassic and Jurassic sediments are also included to have an idea of the vertical variation from Triassic to Jurassic.

Tourmaline is the most abundant transparent heavy mineral that averages 44.3% of the heavy mineral assemblage. It averages 39.8% in the strata below the thick laterite (hereafter called the Triassic strata). In the strata above the thick laterite (hereafter called Jurassic strata), tourmaline averages 51.7% of the total assemblage. Zircon represents the second most abundant transparent heavy mineral and represents 32% of the Triassic heavy mineral population and 29.4% in the Jurassic strata (Figure 14). Rutile constitutes the third most abundant transparent heavy mineral and averages 21.5% of the assemblage (23.9%

in the Triassic and 17.7% in the Jurassic). Staurolite is the least abundant heavy mineral, averaging nearly 3%.

The only visible difference in heavy mineral assemblage is the higher concentration of staurolite in the Triassic strata (averaging 4.1%) that diminished to less than 1% in the Jurassic (Figure 14).

#### 4.5.1. ZTR Index

The sum of total zircons, tourmalines, and rutiles (ZTR) is termed as the ZTR-Index [96]. The lowest ZTR-Index of 87 is measured for the basal unit of the Triassic strata that displays an increasing upsection trend and reaches 100 in the Jurassic strata (Figure 14). The Triassic succession displays an average ZTR-Index of 95.7, while it reaches an average of 98.9 in the overlying Jurassic strata.

#### 4.5.2. Tectonic Setting Using Heavy Minerals Plot

The present sediments lack any of the heavy minerals that can provide evidence for a basic igneous or metamorphic provenance; therefore, the ternary plot of the transport limited (TL) heavy minerals (zircon, tourmaline, rutile)-low grade metamorphic (LGM) heavy minerals (epidote, chloritoid, chlorite, actinolite)-high grade metamorphic (HGM) heavy minerals (sillimanite, staurolite, garnet, andalusite) becomes the ideal candidate for tectonic settings and palaeoclimatic discriminations [97]. Presently, all the samples are clustered near the TL apex of the plot (Figure 15).

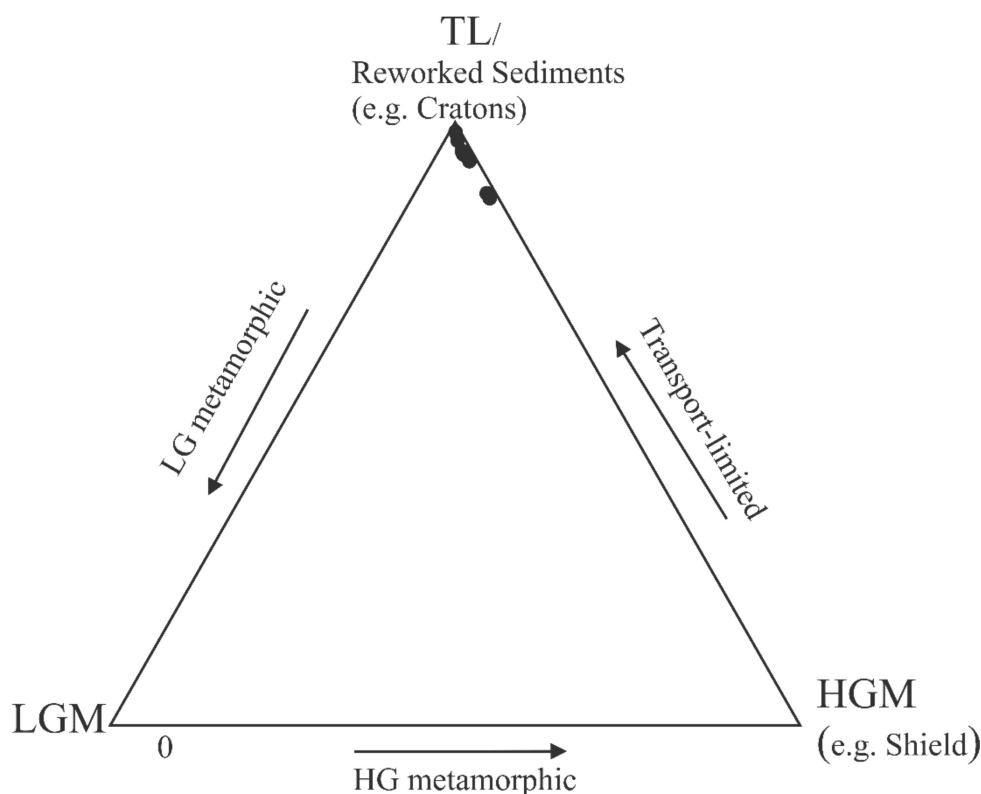


**Figure 15.** Tectonic setting discrimination TL-LGM-HGM heavy minerals plot indicating reworking of sediments in cratonic setting [97]. TL = transport limited; LGM = low grade metamorphic; HGM = high-grade metamorphic.

## 5. Interpretation and Discussion

### 5.1. Sediments Transport Pathways

Restored palaeocurrents data, in combination with the sedimentological characteristics of the investigated strata, advocate for a fluvial system that transported sediments from the palaeo-south-southeast toward the palaeo-north-northwest. The bimodal palaeoflow



suggests the interaction between the fluvial system and the beach/tides [98]. On the other hand, channel avulsion and switching of the meander lobes may also yield bimodal flow [99]. The western Salt Range occupied a comparatively proximal position to the source region, while the Surghar Range was most probably the depocenter of the fluvial-deltaic system. The Khirsor Range (at least the southwestern part) was on the distal side of the depocenter.

## 5.2. Tectonic Settings

### 5.2.1. Quartz–Feldspars–Lithics (QFL) Plots

The pure quartzose nature of the sediments provides evidence for polycyclic nature (Figures 7 and 8) and supports sediment derivation from a stable cratonic interior in a continental block provenance setting [99]. Presently, the concentration of samples in the continental block provenance field (Figure 8b) may negate sediment derivation from magmatic arc source or orogenic belt. Dissolution and differential removal of the liable minerals such as feldspar during weathering produced mature quartz arenite.

### 5.2.2. La/Th versus Hf(ppm) and Ti/Zr versus La/Sc and Nb/La versus (La/Sm)N Plots

Sediments with acidic arc provenance generally have low La/Th ratio and Hf content of about 3–7 ppm [74]. Progressive erosion of the plutonic roots and continental basement of ancient (meta)sedimentary rocks concentrate zircon and hence Hf content in such sediments. The present samples cluster roughly parallel to the Hf axis (Figure 10a). More than 95% of samples support derivation from the acidic arc and passive margin source areas with increasing recycling components. However, possible poor control on the oceanic island arc composition using this plot may question its application. The Ti/Zr versus La/Sc plot [75] addresses this issue.

The oceanic island arc-derived sediments have a higher Ti/Zr ratio (generally > 40) accompanied by a very low La/Sc ratio (<1). The continental island arc detritus displays a Ti/Zr ratio of 10–35 and their La/Sc ratios are 1–3. The active continental margin sediments have Ti/Zr values like the continental island arc, but are discriminated from the latter by their higher La/Sc ratio (3–6). The passive margin siliciclastics have wide variation in their La/Sc ratio, and their low Ti/Zr ratio (generally < 10) discriminate them from sediments of other tectonic settings [75]. The present samples indicate sediment derivation under passive margin setting with a significant component from active continental margin and continental island arc settings (Figure 10b).

The REEs provide significant information in tracing sediment source [100–103]. Oceanic island arc sediments have a high Nb/La ratio and low (La/Sm)N values. The continental arc and passive margin sediments have opposite trends and are positioned parallel to the (La/Sm)N axis [91]. Among these, the passive margin sediments generally have high (La/Sm)N values. The present samples support passive margin settings (Figure 10c).

### 5.2.3. La–Th–Sc, Th–Sc–Zr/10, and Th–Co–Zr/10 Plots

The significance of La/Th and La/Sc values has already been discussed; therefore, repetition is avoided. The Th/Sc ratio is very low (average =  $0.15 \pm 0.08$ ) for the oceanic island arc sediments and these will plot close to the Sc apex. The Th/Sc ratio averages  $0.85 \pm 0.13$  for the continental island arc sediments and  $2.59 \pm 0.5$  for the active continental margin sediments. Sediments derived from passive margin settings have an average Th/Sc ratio of  $3.06 \pm 0.8$  [75].

The La–Th–Sc ternary plot negates oceanic arc-derived sedimentation (Figure 11a). However, with the increasing Th/Sc value, the average error increases. This limitation of the plot does not allow clear discrimination of active continental margin from passive margins. The Zr/Th ratio is helpful in such discriminations. Further, Co behaves concordantly with Sc. Therefore, the Th–Sc–Zr/10 and Th–Co–Zr/10 plots [75] are valuable tools for such discriminations.

The oceanic island arc sediments are depleted in Th, and thus have a high Zr/Th ratio (average =  $48 \pm 13.4$ ) and yield high Th/Sc and Th/Co ratios. Therefore, such sediments

plot close to Sc and Co apices. The Zr/Th ratio for the active continental margin sediments is  $9.5 \pm 0.7$  and is accompanied by low Th/Sc and Th/Co ratios. Hence, such sediments plot in closest vicinity to the Th pole on both plots. The passive margin siliciclastics have a Zr/Th ratio of  $19.1 \pm 5.8$  and their Zr enrichment forces such sediments to plot near the Zr pole. Sediments derived from continental island arc have a Zr/Th average of  $21.5 \pm 2.4$  and on both diagrams occupy an in-between position.

In the present case, the Th–Sc–Zr/10 and Th–Co–Zr/10 plots (Figure 11b,c) support sedimentation of the Datta Formation mostly under passive margin condition. Samples from the Kingriali Formation support sedimentation in an active continental margin and continental island arc source scenario. This apparent difference in sample position is an interplay of the palaeoclimatic conditions. The hot and arid climate during the Rhaetian e.g., [15] probably did not allow the differential leaching of Co [104]; therefore, the Kingriali Formation samples plot away from the passive margin field. The concentration of Co in sediments under reducing conditions [105,106] strengthens this argument. High Zr values in the Datta Formation suggest zircon concentration due to weathering during the Hettangian as interpreted for this time interval in the area and globally e.g., [15]. On the contrary, the transition elements (Co, Ni, and V) are immobile during weathering, and are compatible in magmatic processes. Therefore, Co is highly concentrated in ultramafic and mafic source rocks than felsic rocks [107], and thus mirror the chemistry of their source rocks [108]. Presently, no sediment contribution from oceanic island arc setting is indicated; however, to verify this, the concentration of V and Ni provides valuable information.

### 5.3. Source Compositions Identification

#### V–Ni–Th $\times 10$ and Th/Co versus La/Sc Plots

Mafic source rocks are rich in V and Ni. Therefore, sediments derived from such sources will occupy position along the V–Ni side of the plot. Samples close to Ni-apex support ultramafic source derivation, whereas mafics are close to the V-apex. As felsic sources are rich in Th, such sediments plot close to Th-apex. Presently, the V–Ni–Th  $\times 10$  plot favours sediment derivation from a felsic source (Figure 11d).

The La/Sc versus Th/Co plot [72] provides good discrimination between the acidic and basic source rocks. Generally, Co and Sc are compatible with basic rocks, while La and Th display the opposite trend [73]. Therefore, basic rocks have low La/Sc and Th/Co values. As the felsic sources are rich in Th, sediments derived from these rocks have higher Th/Co ratios. Presently, the La/Sc versus Th/Co plot supports sediment derivation from the silicic composition (Figure 12a).

### 5.4. Weathering and Recycling Trend

#### 5.4.1. Clay Mineralogy

Illite is a common clay mineral in arid climates [109]. Dominance of Illite in the shales of the Kingriali Formation indicates semiarid to arid conditions of deposition during Triassic [110]. The 100% illitic mineralogy of the uppermost green shales of the Kingriali Formation may suggest arid and potentially cooler conditions established during volcanic winters at the start of the Triassic–Jurassic transition [6]. Kaolinite is generally a product of intense chemical weathering, and hence hot and humid climates e.g., [111]. Thus, the kaolinite rich shales of the Datta Formation (Figure 9) support strong chemical weathering during Jurassic. Diagenetic controls generally limit the paleoclimatic significance of clay minerals; however, the sharp change from illite rich clays (in Triassic strata) to kaolinite rich clays (in Jurassic strata) in a confirmable succession supports depositional controls on clay mineralogy [112,113].

#### 5.4.2. CIA and A–CN–K Plots

CIA values may be the direct indication of the intensity of chemical weathering, which is a function of temperature and humidity of the prevailing palaeoclimate [67,68]. CIA values of  $<80$  for the Kingriali Formation (Figure 12d) indicate weak chemical weather-

ing, and thus semiarid to arid palaeoclimate, during the Late Triassic. High CIA values ( $>90$ ) in the Datta Formation favour increased chemical weathering, and thus hot and humid palaeoclimate, during Jurassic. The kaolinite rich clay mineralogy and the presence of laterite/bauxite horizons in the Datta Formation support this palaeoclimatic interpretation [114].

The A–CN–K plot (Figure 12d) is useful in interpreting the weathering trend of sediments [115]. Presently, the sample population between A vertex and muscovite position parallel to the A–K side hints for a recycled origin of the sediments. The muscovite–illite position of samples favours semiarid to arid palaeoclimate for the Kingriali Formation. The cluster of samples close to A apex (kaolinite position) for the Datta Formation indicates increasing chemical maturity, a support of recycling under a hot/warm and humid palaeoclimate. Correlation between the CIA and A–CN–K plot [116] shows coherence between the two data sets (Figure 12d). A possible diagenetic input of carbonates and K-metasomatism may have overprinted the results of CIA and A–CN–K plot, but both of the related corrections have been applied [70].

#### 5.4.3. Th/U versus Th(ppm) and Th/Zr versus Zr/Sc Plots

During weathering, the Th/U value rises above the upper crustal values of 3.5–4.0 [69,111,117]. Sediment weathering and recycling under oxidising conditions results in oxidation of  $U^{4+}$  to  $U^{6+}$ . The  $U^{6+}$  is more soluble and is lost resulting in elevated Th/U ratio e.g., [78,118,119]. Therefore, the Datta Formation (Figure 12b) supports increasing intensity of chemical weathering across the TJB interval into the Hettangian. Low Th/U values in the Kingriali Formation indicate poor chemical weathering during the Rhaetian.

Zr is particularly enriched in zircons, while Sc generally preserves its provenance signature; therefore, the Zr/Sc ratio is a useful index of zircon enrichment [120]. The incompatibility of Th makes Th/Sc a good indicator of igneous chemical differentiation processes. Presently, the higher Zr/Sc and Th/Sc ratios indicate increasing weathering and sediment recycling from the Kingriali Formation to the Datta Formation (Figure 12c).

#### 5.5. Heavy Minerals and Weathering and Tectonics

Heavy mineral analyses have a wide range of applications in studying the provenance of siliciclastic rocks e.g., [121]. Specific heavy minerals assemblages are a characteristic of specific source rocks and are sensitive indicators of provenance [122]. The dominance of ultra-stable heavy minerals (zircon, tourmaline, and rutile, i.e., high ZTR  $> 87$ ) supports the differential removal of chemically unstable minerals under multi-cyclic weathering, erosion, and transportation. The presence of well-preserved crystals (Figure 13a,b) in the Triassic strata does not support rounding and thus long transportation. Their relatively small grain-sizes (Figure 14) further hint for the absence of high energy transporting agent. The presence of sharp edges and lack of corroded margins and dissolution cavities may negate strong chemical weathering (Figure 13b). The presence of staurolite suggests derivation from a nearby metamorphic source.

The rounded to very well rounded heavy mineral assemblage of the Jurassic strata supports an efficient transport mechanism. This supports hydraulic sorting during fluvial transport under prolonged exposure of the low-relief source areas. The relatively coarse-grained nature of these minerals indicates high energy transporting agent. The corroded and etched grains indicate strong chemical weathering (Figure 13a).

The concentration of ultra-stable heavy mineral suites (ZTR) suggests extensive recycling with no contemporaneous volcanic activity. The corroded margins in the Jurassic heavy minerals could hint for dissolution and differential removal of the liable heavy minerals during diagenesis. However, the presence of well-preserved crystals in the Triassic strata does not favour deep burial diagenesis.

The cluster of samples along the TL apex (Figure 15) indicates sediment derivation from a mature and recycled source such as passive margins, cratonic basins, and craton

lowlands. Additionally, such mature quartz-rich sediments may indicate uplift and erosion of mature sedimentary rocks [97].

#### 5.6. Palaeogeography and Possible Detritus Suppliers

The neo-Proterozoic (800 Ma to 600 Ma) marks the peak time of crust production during the Pan-African Orogeny prior to the assembly of Gondwana [123]. Geochronology of the Pan-African orogenic belts in the central-north Africa, Saudi Arabia, Kazakhstan, eastern Baltica, and Pakistan Block supports continental crust formation during this period. The final Gondwana assembly occurred at ca. 540 Ma and, by the late Cambrian (ca. 500 Ma), the orogeny had produced sufficient positive relief structures in Arabia, East Africa, as well in Pakistan that could have provided the long-term source for sedimentary basins [123].

The palaeogeographic position [90] of the study area (Figure 16a,b) puts the nearby Arabian Plate, Greater Somalian Plate (southeastern margin of northeastern Africa), and Indian Plate as the candidate sources of the siliciclastics. The Arabian–Nubian Shield in these areas formed during the Pan-African Orogeny, closure of Mozambique Ocean, and subsequent collision of east and west Gondwana at ca. 540 Ma [124]. The basement rocks of Arabian Peninsula include amphibolite facies gneissic terrains, diorites, tonalites, and granitoids, as well as granites with rhyolites, tuffs, lava breccias, quartzites, marbles, and mafic dykes [125]. Similar gneisses, basalts, tuffs, rhyolites, granites, quartzites, and marbles also occur in Somalia [126]. However, both the pinching out of the strata and decreasing grain size towards the west-northwest and south-southwest [40] negate siliciclastic supply from the Arabian and Greater Somalian plates. Further, the palaeoflow direction (Figure 5) argues against sediment supply from these two sites and advocate for an easterly (present-day) source of the sediments. Thus, the Indian Plate most likely served as the principal source for the siliciclastics (Figures 16c and 17).

#### 5.7. Correlation with Northern Indian Passive Tethyan Margin

The Salt Range (Kohat-Potwar Basin) represents a rim basin along the NW margin of India (Figure 16c) associated with the Neo-Tethys rift system [127]. It possibly opened into a rift that separated Arabia and India, which extended towards Madagascar [128] and connected southwards up with the Karoo system [129]. The rifting activity most likely commenced during the Late Carboniferous [16,19,42]. Evidence for various stages of the Neo-Tethys opening in SRS and their tentative correlation with the THS is provided in the

Geological setting and palaeogeography chapter (Table 1) and an extended correlation between the syn-rift and drift sequences of the THS and the SRS is presented here.

The syn-rift sequence in the THS includes the Pennsylvanian to lowermost Permian glacial diamictites overlain by Sakmarian deglaciation mudrocks [130]. The glacial diamictites of the Tobra Formation e.g., [45] and the overlying deglaciation shale/mudrocks of the Dandot Formation with cold water Eurydesma fauna [40] of Gondwanan characters may be an indication of the westward extension of the synrift sequence in the SRS. A gentle angular unconformity (1–2°) exists between the Tobra Formation and the underlying Cambrian strata (Figure 2) in the Salt Range [131]. This correlates with the angular unconformity between Upper Devonian to Tournaisian limestones and the overlying rift sequence in the THS [132]. Furthermore, normal faults in the strata underlying the Tobra Formation are observed in the field and reported in the basement on seismic data e.g., [47] that provide additional evidence for rift-related tectonics in the Salt Range area like those observed in THS e.g., [133].

The “break-up unconformity” on top of the rift sequence observed in THS (Lahul-Zanskar) [21] is not truly reported in the SRS. However, the Dandot Formation (uppermost part of the syn-rift sequence) is missing in the western Salt Range and in the Khisor Range [40]. The basal part of the drift sequence in the Salt Range consists of Permian sands and shales (Warchha and Sardhai formations) overlain by limestones (Zaulch Group) and displays an overall transgressive trend like that observed in the Lahul-Zanskar area (THS)



e.g., [21]. The presence of Lower Triassic ammonoid-rich sediments (Mianwali Formation) in the Salt Range e.g., [47] may indicate subsidence of the newly formed rift margin and correlates with the ammonoid-rich sediments of THS deposited in Lower Triassic [134,135]. Thick sandstones of the Tredian Formation succeed the Mianwali Formation [47]. This may provide evidence for the sudden increase in siliciclastic supply in the Salt Range during the Middle–Late Triassic like that observed in the THS [136]. Large-scale syn-depositional slumps occur especially in the lower part of the Tredian Formation [47]. These slumps provide evidence for possible occurrence of tectonic activity in the Salt Range like passive margin rejuvenation observed in the THS. The present quartz-rich sediments of the Kingriali and Datta formations in the Salt Range during the Late Triassic to Early Jurassic [15] may correlate with the deposition of quartzose sands until the middle Early Jurassic in the THS [22]. In the Salt Range the platform carbonates of the Samana Suk Formation were deposited following the Datta Formation and reflect the mature passive-margin stage of the Neo-Tethys as observed by carbonate-platform sedimentation during the mature passive-margin stage in the THS [23].

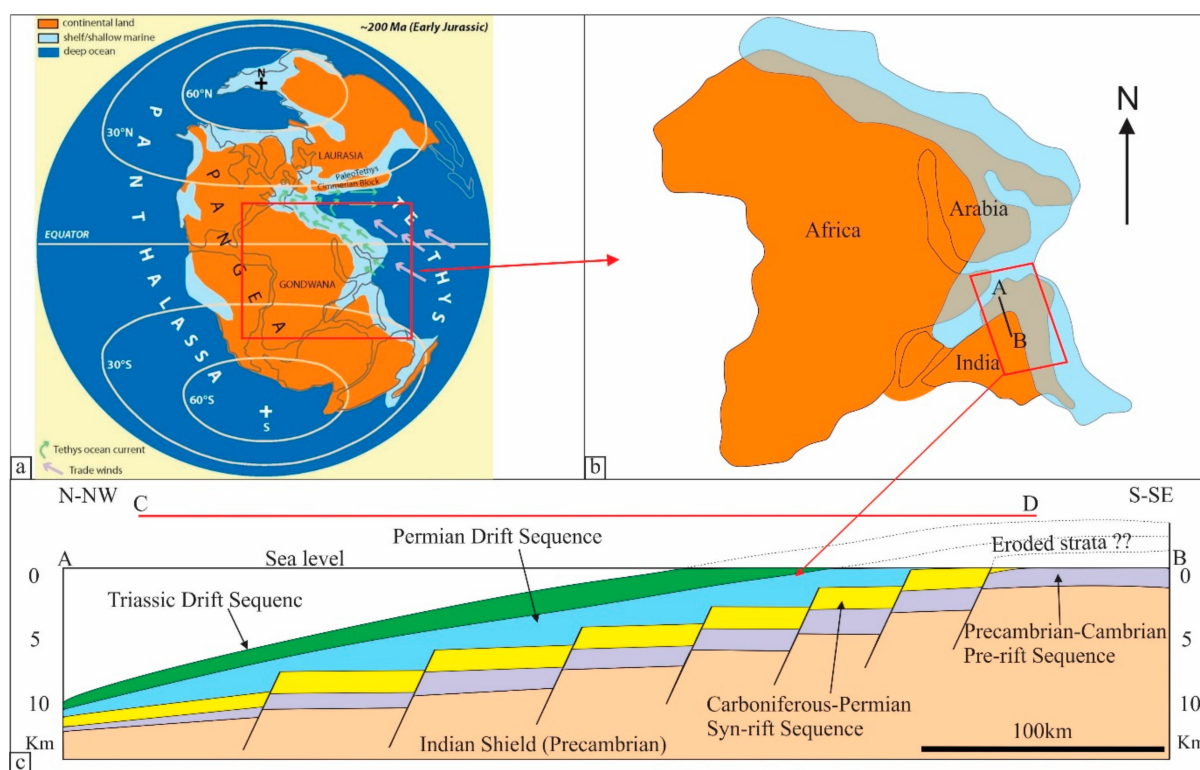


**Figure 16.** (a,b) Palaeogeographic position of the Salt and Trans–Indus ranges during the TJB interval with location of cross section A–B [90]; and (c) tentative basin cross-section A–B of the northwestern passive margin of the Indian Plate during Late Triassic (modified from [42]) with pre-rift, syn-rift, and drift sequences marked e.g., [16]. Location of cross section C–D (explained in Figure 17) is also given.

The break-up of Gondwana and formation of NW passive margin of the India began in Late Carboniferous, around 100 ma prior to the deposition of the sediments under study e.g., [137]. By the Late Triassic, passive margin setting had established in the area now the Salt Range. A possible faulting and tilting of strata during passive margin rejuvenation occurred during this time [16,136,138,139]. These complicated processes probably resulted in the post-break-up exhumation of the passive margin in the eastern Salt Range and adjoining areas e.g., [140,141]. The prominent sea-level fall observed at the TJB interval in the Salt Range and globally [9–11,15] may also have facilitated exposure in the eastern Salt Range. This passive margin exhumation and subsequent exposure of the Triassic and older strata in the Salt Range and further south-southeast in Greater India may have provided

the main source for sediments that were transported north-northwestward by the newly established fluvial system during the Late Triassic–Early Jurassic (Figure 17).

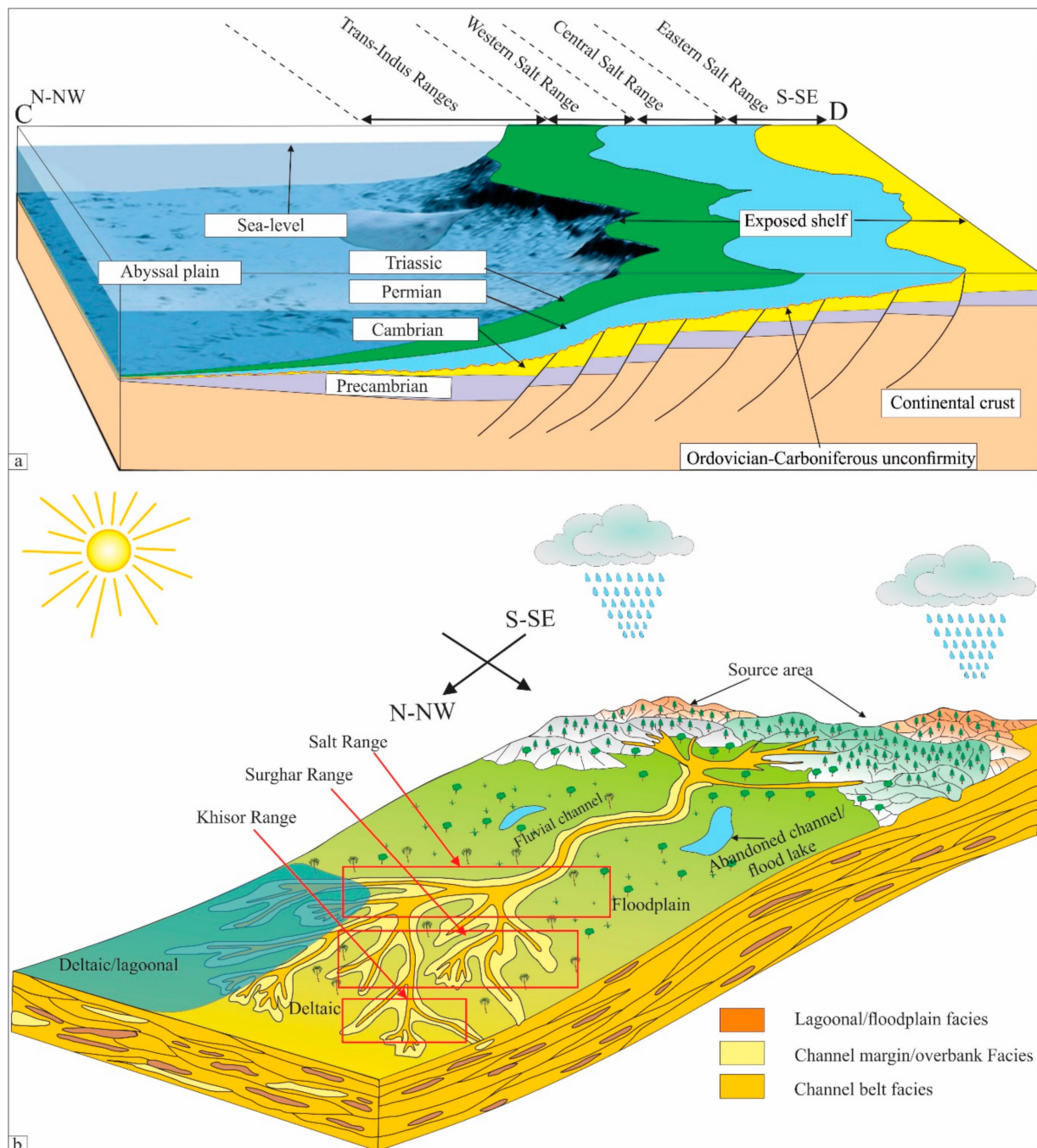


**Figure 17.** (a) A cross-sectional C–D (see Figure 16 for location) view of the northwestern margin of the Indian Plate ca. 200 Ma ago; (b) source to sink transport model for the Upper Triassic–Lower Jurassic siliciclastics in the Salt and Trans-Indus ranges. Note: both models are not to scale.

### 5.8. Possible Sediment Suppliers

The north-south trending, nearly 700 km long, Aravalli–Malani Range (Figure 18) is a part of the foreland normal-sense high strain zones that were active in the Paleoproterozoic [142]. The range is located 600 km to the southeast of the Salt Range and was a positive topographic feature by Early Permian [43]. The Precambrian Aravalli Supergroup

overlies the banded gneisses [143] and consists of granites, siliciclastics, carbonates, slates, and phyllites [144]. The Malani Suite consists of porphyritic rhyolites and granites [145].

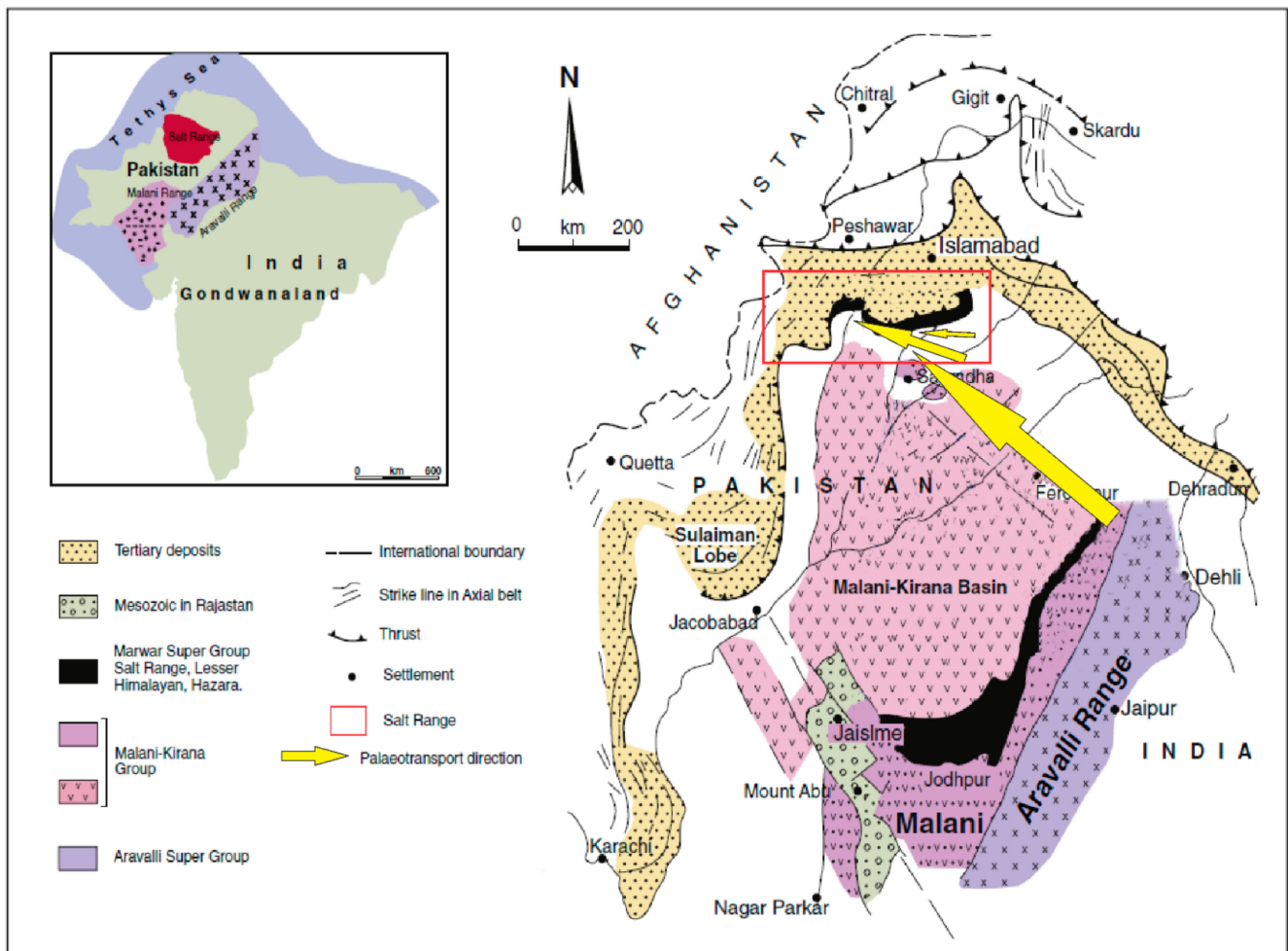


**Figure 18.** A generalised geological map of foreland Pakistan and adjoining northwest India showing the Salt Range and the possible source areas of the siliciclastics for the Upper Triassic–Lower Jurassic siliciclastics of the Kingriali and Datta formations (modified from [43]).

The rhyolites have abundant pink orthoclase and some sanidine, oligoclase, quartz, and rare hornblende and magnetite. The pink coloured Malani Granite intruded the rhyolites and is composed of orthoclase, quartz, sodic plagioclase, biotite, hornblende, and less common occurrences of muscovite. Accessory minerals include tourmaline and fluorite.

The Lower Permian, glacial–periglacial Tobra Formation in the Salt Range contains lithoclasts of Aravalli–Malani origin [45]. Similarly, the same ranges shed detritus for the Permian Warchha Sandstone of the Salt Range. Further, the sedimentary clasts within the Warchha Sandstone are considered to have been the product of local recycling of the underlying Permian, Cambrian, and Precambrian strata in the Salt Range region itself [43].

The Salt Range contains thick Cambrian, Permian, and Triassic siliciclastics that could prove detritus suppliers if exposed to surficial weathering and denudation. These include the thick sandstones and shales of the Cambrian Khewra Sandstone (sandstones), Kussak Formation (sandstones and shale), and Baghanwala Formation (sandstones, shales). The Lower Permian Nilawahana Group in the area consists of thick conglomerates of Tobra Formation, shales of Dandot Formation, sandstones and shales of Warchha Sandstone, and shales of Sardhai formations. The shales and sandstones of Mianwali Formation and the thick sandstones of Tredian Formation constitute the Triassic siliciclastics in the Salt



Range [40,43]. Exposure of these Triassic and older sediments of the Salt Range itself during the eastward exhumation of the passive margin may have provided siliciclastic detritus for the Triassic–Jurassic sediments of the western Salt Range and adjoining area. The tropical palaeogeographic position of the area favoured dissolution of the liable components, thereby producing highly mature quartz arenites [15]. The comparative low relief did not allow sediment derivation from diverse source rocks. The meandering fluvial system reworked and transported mostly the older Triassic and Permian siliciclastics (Figure 17a) [146].

This is confirmed by the eastward disappearance of the Triassic and Permian strata in the present-day eastern Salt Range (Figure 2). A possible destruction of the unstable minerals during diagenesis may have further facilitated the formation of quartz arenites [147–150]. However, lack of evidence does not allow reliable understanding of the diagenetic history of the present sediments, while the recently published burial history of the area [131] does not indicate deep burial of the strata during Mesozoic.

The extreme wet greenhouse conditions interpreted for the Jurassic strata [15,57,58] could have easily removed unstable components, thereby forcing highly mature quartz arenites with very high ZTR-index and hiding evidence for sediment incorporation from the basement or other diverse sources. However, Cambrian and older strata are widely distributed throughout the Salt and Trans–Indus ranges (Figure 17a) and reported in the subsurface in the Kohat–Potwar Plateau and Punjab platform [40], thereby indicating that the fluvial system was unable to cut into the Cambrian and older strata and the basement rocks were not exposed to reworking.

## 6. Conclusions

The Neo-Tethys opening produced passive margin settings on the north-northwestern margin of the Indian Plate. Tectonic activity during this passive margin formation produced elevated passive margin in the eastern Salt Range and area further to the east on the Indian Plate. A prominent sea-level fall and a possible passive margin rejuvenation in the area during the late Triassic resulted in the demise of the Rhaetian platform carbonates deposition and a fluvial system initiated during the TJB interval in the Salt and Trans–Indus ranges. During the following Hettangian, this system matured into a fluvio-deltaic system under wet greenhouse palaeoclimatic conditions and had a general south-southeast to north-northwest palaeoflow. The present analyses do not support direct sediment derivation from the Indian Plate basement rocks. Instead, the fluvial system reworked the older (Carboniferous–Permian–Triassic) strata in the present-day eastern Salt Range and adjoining western-northwestern part of the Indian Plate. These polycyclic sediments were deposited (as the upper part of the Kingriali Formation and the Datta Formation) in the western Salt Range and Trans–Indus ranges in a fluvio-deltaic depositional system in a Neo-Tethyan passive margin setting like that observed in the Tethyan Himalaya. Thus, the Triassic–Jurassic sediments of the Salt and Trans Indus ranges, Pakistan, provide evidence for westward extension of the Neo-Tethyan passive margin and possible occurrence of Tethyan Himalayan Succession in the Salt Range. Varietal studies and isotopic geochronology are suggested to be carried to further pinpoint the source rock for these sediments.

**Supplementary Materials:** The following are available online at <https://www.mdpi.com/article/10.3390/min11060573/s1>. Supplementary Materials S1. Point counting data for framework mineralogical composition of the selected samples.  $Q_{muc}$  = monocrystalline quartz with unit extinction,  $Q_{muu}$  = monocrystalline quartz with undulose extinction,  $Q_{pq}$  = polycrystalline quartz including chert,  $Q_{total}$  = total quartz, A = K-feldspar, P = plagioclase,  $F_{total}$  = total feldspar,  $L_v$  = volcanic and hypabyssal lithic,  $L_m$  = metamorphic lithic,  $L_s$  = sedimentary lithic excluding chert,  $L_{total}$  = total lithic, M = phyllosilicates, D = heavy minerals, O = others/not recognizable. Supplementary Materials S2. Bulk rock geochemistry data for the selected samples. The concentration of major oxides/elements is provided in percentage (%), while trace element concentrations are listed in parts per million



(ppm). Note that only those chemical species are included here that are used in the present study. Supplementary Materials S3. Point count data for heavy minerals of the selected samples.

**Author Contributions:** Conceptualization, S.I. and M.W.; Data curation, M.B. and I.U.J.; Formal analysis, S.I., M.B. and S.G.; Funding acquisition, S.I. and M.W.; Investigation, S.I. and I.U.J.; Methodology, S.I. and S.G.; Project administration, M.W.; Resources, M.W. and I.U.J.; Software, S.I. and M.B.; Validation, S.I. and S.G.; Visualization, S.I. and M.W.; Writing—original draft, S.I.; Writing—review & editing, S.I. and M.W. All authors have read and agreed to the published version of the manuscript.

**Funding:** This research was funded by UNESCO-IUGS project IGCP-609 and Higher Education Commission (HEC) Pakistan.

**Institutional Review Board Statement:** Not applicable.

**Informed Consent Statement:** Not applicable.

**Data Availability Statement:** Data are available in Supplementary Materials.

**Acknowledgments:** The authors are thankful to Hafiz Shahid Hussain, Mukhtiar Ghani, and Syed Irfan Hashmi for their help during the fieldwork. Claudia Beybel and Ilka Wünsche provided technical support in thin-section preparation and Maria Meszar and Sabine Hruby-Nichtenberger helped in heavy minerals sample preparation. Comments of three anonymous reviewers greatly improved quality of the manuscript.

**Conflicts of Interest:** The authors declare no conflict of interest.

## References

- Schlische, R.W.; Withjack, M.O.; Olsen, P.E. Relative timing of CAMP, rifting, continental breakup, and basin inversion: Tectonic significance. In *The Central Atlantic Magmatic Province, Insights from Fragments of Pangea*; Geophysical Monograph; Hames, W.E., McHone, J.G., Renne, P.R., Ruppel, C., Eds.; American Geophysical Union: Washington, DC, USA, 2003; Volume 136, pp. 33–59. [\[CrossRef\]](#)
- De Lamotte, D.F.; Fourdan, B.; Leleu, S.; Leparmentier, F.; De Clarens, P. Style of rifting and the stages of Pangea breakup. *Tectonics* **2015**, *34*, 1009–1029. [\[CrossRef\]](#)
- Peace, A.L.; Phethean, J.; Franke, D.; Foulger, G.; Schiffer, C.; Welford, J.; McHone, G.; Rocchi, S.; Schnabel, M.; Doré, A. A review of Pangaea dispersal and Large Igneous Provinces—In search of a causative mechanism. *Earth Sci. Rev.* **2020**, *206*, 102902. [\[CrossRef\]](#)
- Withjack, M.O.; Schlische, R.W.; Olsen, P.E. Diachronous rifting, drifting, and inversion on the passive margin of central eastern North America: An analog for other passive margins. *AAPG Bull.* **1998**, *82*, 817–835.
- Marzoli, A.; Renne, P.R.; Piccirillo, E.M.; Ernesto, M.; Bellieni, G.; De Min, A. Extensive 200-Million-Year-Old Continental Flood Basalts of the Central Atlantic Magmatic Province. *Science* **1999**, *284*, 616–618. [\[CrossRef\]](#) [\[PubMed\]](#)
- Olsen, P.E. Giant lava flows, mass extinctions, and mantle plumes. *Science* **1999**, *284*, 604–605. [\[CrossRef\]](#)
- Petersen, K.D.; Schiffer, C. Wilson cycle passive margins: Control of orogenic inheritance on continental breakup. *Gondwana Res.* **2016**, *39*, 131–144. [\[CrossRef\]](#)
- Sepkowski, J.J. Biodiversity: Past, present, and future. *J. Paleontol.* **1997**, *71*, 533–539. [\[CrossRef\]](#) [\[PubMed\]](#)
- Hallam, A. A review of the broad pattern of Jurassic sea-level changes and their possible causes in the light of current knowledge. *Palaeogeogr. Palaeoclim. Palaeoecol.* **2001**, *167*, 23–37. [\[CrossRef\]](#)
- Haq, B.U. Jurassic Sea-Level Variations: A Reappraisal. *GSA Today* **2017**, *28*, 4–10. [\[CrossRef\]](#)
- Hallam, A. Mass extinctions and sea-level changes. *Earth Sci. Rev.* **1999**, *48*, 217–250. [\[CrossRef\]](#)
- Ludwig, W.; Amiotte-Suchet, P.; Probst, J.-L. Enhanced chemical weathering of rocks during the last glacial maximum: A sink for atmospheric CO<sub>2</sub>? *Chem. Geol.* **1999**, *159*, 147–161. [\[CrossRef\]](#)
- Hallam, T.; Wignall, P.; Hesselbo, S.P.; Robinson, S.A.; Surlyk, F. Discussion on sea-level change and facies development across potential Triassic–Jurassic boundary horizons, SW Britain. *J. Geol. Soc.* **2004**, *161*, 1053–1056. [\[CrossRef\]](#)
- Zajzon, N.; Kristály, F.; Pálffy, J.; Németh, T. Detailed clay mineralogy of the Triassic–Jurassic boundary section at Kendlbachgraben (Northern Calcareous Alps, Austria). *Clay Miner.* **2012**, *47*, 177–189. [\[CrossRef\]](#)
- Iqbal, S.; Wagreich, M.; Irfan U, J.; Kuerschner, W.M.; Gier, S.; Bibi, M. Hot-house climate during the Triassic/Jurassic transition: The evidence of climate change from the southern hemisphere (Salt Range, Pakistan). *Glob. Planet. Chang.* **2019**, *172*, 15–32. [\[CrossRef\]](#)
- Sciunnach, D.; Garzanti, E. Subsidence history of the Tethys Himalaya. *Earth Science Rev.* **2012**, *111*, 179–198. [\[CrossRef\]](#)
- Yin, A.; Harrison, T.M. Geologic Evolution of the Himalayan–Tibetan Orogen. *Annu. Rev. Earth Planet. Sci.* **2000**, *28*, 211–280. [\[CrossRef\]](#)
- Yin, A. Cenozoic tectonic evolution of the Himalayan orogen as constrained by along-strike variation of structural geometry, exhumation history, and foreland sedimentation. *Earth Sci. Rev.* **2006**, *76*, 1–131. [\[CrossRef\]](#)

19. Zhang, B.; Wei, Y.; Garzanti, E.; Wang, C.; Chen, X.; Pan, W.; Liu, Q. Sedimentologic and stratigraphic constraints on the orientation of the Late Triassic northern Indian passive continental margin. *Palaeogeogr. Palaeoclim. Palaeoecol.* **2019**, *533*, 109234. [[CrossRef](#)]
20. Gaetani, M.; Garzanti, E. Multicyclic history of the Northern India continental margin (Northwestern Himalaya) (1). *Am. Assoc. Pet. Geol. Bull.* **1991**, *75*, 1427–1446.
21. Garzanti, E.; Angiolini, L.; Sciunnach, D. The Permian Kuling Group (Spiti, Lahaul and Zaskar; NW Himalaya): Sedimentary evolution during rift/drift transition and initial opening of neo-tethys. *Riv. Ital. Paleontologia Stratigr.* **1996**, *102*, 175–200.
22. Jadoul, F.; Berra, F.; Garzanti, E. The Tethys Himalayan passive margin from Late Triassic to Early Cretaceous (South Tibet). *J. Asian Earth Sci.* **1998**, *16*, 173–194. [[CrossRef](#)]
23. Garzanti, E. Stratigraphy and sedimentary history of the Nepal Tethys Himalaya passive margin. *J. Asian Earth Sci.* **1999**, *17*, 805–827. [[CrossRef](#)]
24. DeCelles, P.G. Tectonic Implications of U-Pb Zircon Ages of the Himalayan Orogenic Belt in Nepal. *Science* **2000**, *288*, 497–499. [[CrossRef](#)]
25. McQuarrie, N.; Robinson, D.; Long, S.; Tobgay, T.; Grujic, D.; Gehrels, G.; Ducea, M. Preliminary stratigraphic and structural architecture of Bhutan: Implications for the along strike architecture of the Himalayan system. *Earth Planet. Sci. Lett.* **2008**, *272*, 105–117. [[CrossRef](#)]
26. McQuarrie, N.; Long, S.; Tobgay, T.; Nesbit, J.; Gehrels, G.E.; Ducea, M.N. Documenting basin scale, geometry and provenance through detrital geochemical data: Lessons from the Neoproterozoic to Ordovician Lesser, Greater, and Tethyan Himalayan strata of Bhutan. *Gondwana Res.* **2013**, *23*, 1491–1510. [[CrossRef](#)]
27. Myrow, P.M.; Hughes, N.C.; Goodge, J.; Fanning, C.M.; Williams, I.S.; Peng, S.; Bhargava, O.N.; Parcha, S.K.; Pogue, K.R. Extraordinary transport and mixing of sediment across Himalayan central Gondwana during the Cambrian-Ordovician. *GSA Bull.* **2010**, *122*, 1660–1670. [[CrossRef](#)]
28. Gehrels, G.; Kapp, P.; DeCelles, P.; Pullen, A.; Blakey, R.; Weislogel, A.; Ding, L.; Guynn, J.; Martin, A.; McQuarrie, N.; et al. Detrital zircon geochronology of pre-Tertiary strata in the Tibetan-Himalayan orogen. *Tectonics* **2011**, *30*, 1–27. [[CrossRef](#)]
29. Zhu, D.-C.; Zhao, Z.-D.; Niu, Y.; Dilek, Y.; Hou, Z.-Q.; Mo, X.-X. The origin and pre-Cenozoic evolution of the Tibetan Plateau. *Gondwana Res.* **2013**, *23*, 1429–1454. [[CrossRef](#)]
30. Gaetani, M.; Casnedi, R.; Fois, E.; Garzanti, E.; Jadoul, F.; Nicora, A.; Tintori, A. Stratigraphy of the Tethys Himalaya in Zaskar, Ladakh. *Riv. Ital. Paleontol. Stratigr.* **1986**, *91*, 443–478.
31. Jadoul, F.; Garzanti, E.; Fois, E. Upper Triassic-Lower Jurassic stratigraphy and palaeogeographic evolution of the Zaskar Tethys Himalaya (Zangla Unit). *Riv. Ital. Paleontologia Stratigr.* **1990**, *95*, 351–396. [[CrossRef](#)]
32. Ali, J.R.; Aitchison, J.C. Greater India's northern margin prior to its collision with Asia. *Basin Res.* **2014**, *26*, 73–84. [[CrossRef](#)]
33. Bhargava, O.N. Evolution of the Tethyan and Karewa successions in Kashmir: A synthesis. *J. Paleontol. Soc. India* **2015**, *60*, 51–71.
34. Rees, P.M.; Ziegler, A.M.; Valdes, P.J. Jurassic phytogeography and climates: New data and model comparisons. In *Warm Climates in Earth History*; Huber, B.T., Macleod, K.G., Wing, S.L., Eds.; Cambridge University Press: Cambridge, UK, 2000; pp. 297–318.
35. Faisal, S.; Dixon, J.M. Physical analog (centrifuge) model investigation of contrasting structural styles in the Salt Range and Potwar Plateau, northern Pakistan. *J. Struct. Geol.* **2015**, *77*, 277–292. [[CrossRef](#)]
36. Iqbal, S.; Jan, I.U.; Akhter, M.G.; Bibi, M. Palaeoenvironmental and sequence stratigraphic analyses of the Jurassic Datta Formation, Salt Range, Pakistan. *J. Earth Syst. Sci.* **2015**, *124*, 747–766. [[CrossRef](#)]
37. Kadri, I.B. *Petroleum Geology of Pakistan*; Pakistan Petroleum Limited: Karachi, Pakistan, 1995; p. 275.
38. Kazmi, A.H.; Jan, M.Q. *Geology and Tectonic of Pakistan*; Graphic Publication: Karachi, Pakistan, 1997; p. 554.
39. Kazmi, A.H.; Abbasi, I.A. *Stratigraphy & Historical Geology of Pakistan*; Department and National Centre of Excellence in Geology: Peshawar, Pakistan, 2008; p. 524.
40. Shah, S.M.I. *Stratigraphy of Pakistan*; Gov Pak Ministry of Petroleum and Natural Resources Geological Survey of Pakistan: Islamabad, Pakistan, 2009; p. 381.
41. Hassan, S.; Ishiga, H.; Roser, B.; Dozen, K.; Naka, T. Geochemistry of Permian–Triassic shales in the Salt Range, Pakistan: Implications for provenance and tectonism at the Gondwana margin. *Chem. Geol.* **1999**, *158*, 293–314. [[CrossRef](#)]
42. Stampfli, G.M.; Mosar, J.; Favre, P.; Pillevert, A.; Vannay, J.C. Permo-Mesozoic evolution of the western Tethys realm: The Neo-Tethys East Mediterranean Basin connection. In *Peri-Tethys Memoir 6: Peri-Tethyan Rift/Wrench Basins and Passive Margins*; Ziegler, P.A., Cavalza, W., Robertson, A.H.F., Crasquin-Soleau, S., Eds.; Mémoires du Muséum National D'histoire Naturelle: Paris, France, 2001; Volume 186, pp. 51–108. ISBN 2-85653-528-3.
43. Ghazi, S.; Mountney, N.P. Petrography and provenance of the Early Permian Fluvial Warchha Sandstone, Salt Range, Pakistan. *Sediment. Geol.* **2011**, *233*, 88–110. [[CrossRef](#)]
44. Jehangiri, M.; Hanif, M.; Arif, M.; Jan, I.U.; Ahmad, S. The Early Cambrian Khewra Sandstone, Salt Range, Pakistan: Endorsing southern Indian provenance. *Arab. J. Geosci.* **2014**, *8*, 6169–6187. [[CrossRef](#)]
45. Jan, I.U.; Iqbal, S.; Davies, S.J.; Zalasiewicz, J.A.; Stephenson, M.H.; Wagerich, M.; Haneef, M.; Hanif, M.; Ahmad, S. A Periglacial Palaeoenvironment in the Upper Carboniferous-Lower Permian Tobra Formation of the Salt Range, Pakistan. *Acta Geol. Sin.* **2017**, *91*, 1063–1078. [[CrossRef](#)]
46. Burbank, D.W.; Reynolds, R.G.H. Stratigraphic keys to the timing of thrusting in the terrestrial foreland basins: Applications to the northwest Himalaya. In *Frontiers in Sedimentary Geology, New Perspective in Basin Analysis*; Kleinspahn, K.L., Paol, C., Eds.; Springer: Berlin, Germany, 1988; pp. 331–351.

47. Iqbal, S.; Jan, I.U.; Hanif, M. The Mianwali and Tredian Formations: An Example of the Triassic Progradational Deltaic System in the Low-Latitude Western Salt Range, Pakistan. *Arab. J. Sci. Eng.* **2013**, *39*, 5489–5507. [[CrossRef](#)]
48. Iqbal, S.; Akhter, G.; Bibi, S. Structural model of the Balkassar area, Potwar Plateau, Pakistan. *Acta Diabetol.* **2015**, *104*, 2253–2272. [[CrossRef](#)]
49. Wiesmayr, G.; Grasemann, B. Eohimalayan fold and thrust belt: Implications for the geodynamic evolution of the NW-Himalaya (India). *Tectonics* **2002**, *21*. [[CrossRef](#)]
50. Bhargava, O.N.; Frank, W.; Bertle, R. Late Cambrian deformation in the Lesser Himalaya. *J. Asian Earth Sci.* **2011**, *40*, 201–212. [[CrossRef](#)]
51. Klootwijk, C.T.; Gee, J.S.; Peirce, J.W.; Smith, G.M.; McFadden, P.L. An early India-Asia contact: Paleomagnetic constraints from Ninetyeast Ridge, ODP Leg 121. *Geology* **1992**, *20*, 395–398. [[CrossRef](#)]
52. Dupont-Nivet, G.; Lippert, P.C.; Van Hinsbergen, D.J.; Meijers, M.J.; Kapp, P. Palaeolatitude and age of the Indo-Asia collision: Palaeomagnetic constraints. *Geophys. J. Int.* **2010**, *182*, 1189–1198. [[CrossRef](#)]
53. Najman, Y.; Appel, E.; BouDagher-Fadel, M.; Bown, P.; Carter, A.; Garzanti, E.; Godin, L.; Han, J.; Liebke, U.; Oliver, G.; et al. Timing of India-Asia collision: Geological, biostratigraphic, and palaeomagnetic constraints. *J. Geophys. Res. Space Phys.* **2010**, *115*, 12416. [[CrossRef](#)]
54. Damborenea, S.E. Jurassic evolution of Southern Hemisphere marine palaeobiogeographic units based on benthonic bivalves. *Geobios* **2002**, *35*, 51–71. [[CrossRef](#)]
55. Scotese, C.R. *Atlas of Jurassic Paleogeographic Maps, PALEOMAP Atlas for ArcGIS; The Jurassic, Maps 32–42, Mollweide Projection; PALEOMAP Project: Evanston, IL, USA, 2014; Volume 4.*
56. Ge, Y.; Al-Suwaidi, A.; Shi, M.; Li, Q.; Morad, S.; Steuber, T. Short-term variation of ooid mineralogy in the Triassic-Jurassic boundary interval and its environmental implications: Evidence from the equatorial Ghalilah Formation, United Arab Emirates. *Glob. Planet. Chang.* **2019**, *182*, 103006. [[CrossRef](#)]
57. Hesselbo, S.P.; Korte, C.; Ullmann, C.V.; Ebbesen, A.L. Carbon and oxygen isotope records from the southern Eurasian Seaway following the Triassic-Jurassic boundary: Parallel long-term enhanced carbon burial and seawater warming. *Earth Sci. Rev.* **2020**, *203*, 103131. [[CrossRef](#)]
58. Ruhl, M.; Hesselbo, S.; Al-Suwaidi, A.; Jenkyns, H.; Damborenea, S.; Manceñido, M.; Storm, M.; Mather, T.; Riccardi, A. On the onset of Central Atlantic Magmatic Province (CAMP) volcanism and environmental and carbon-cycle change at the Triassic–Jurassic transition (Neuquén Basin, Argentina). *Earth Sci. Rev.* **2020**, *208*, 103229. [[CrossRef](#)]
59. Collinson, J.; Mountney, N.; Thompson, D. *Sedimentary Structures*; Terra Publishing: London, UK, 2006.
60. Dickinson, W.R.; Beard, L.S.; Brakenridge, G.R.; Erjavec, J.L.; Ferguson, R.C.; Inman, K.F.; Knepp, R.A.; Lindberg, F.A.; Ryberg, P.T. Provenance of North American Phanerozoic Sandstones in Relation to Tectonic Setting. *Geol. Soc. Am. Bull.* **1983**, *94*, 222–235. [[CrossRef](#)]
61. Ingersoll, R.V.; Bullard, T.F.; Ford, R.L.; Grimm, J.P.; Pickle, J.D.; Sares, S.W. The effect of grain size on detrital modes: A test of the Gazzi-Dickinson point-counting method. *J. Sediment. Res.* **1984**, *54*, 103–116. [[CrossRef](#)]
62. Garzanti, E. Petrographic classification of sand and sandstone. *Earth Sci. Rev.* **2019**, *192*, 545–563. [[CrossRef](#)]
63. Van Langeveld, A.D.; Van der Gaast, S.J.; Eisma, D. A comparison of the effectiveness of eight methods for the removal of organic matter from clay. *Clays Clay Miner.* **1978**, *26*, 361–364. [[CrossRef](#)]
64. Moore, D.M.; Reynolds, R.C., Jr. *X-ray Diffraction and the Identification and Analysis of Clay Minerals*; Oxford University Press (OUP): Oxford, UK, 1989.
65. Brindley, G.W.; Brown, G. Quantitative X-ray mineral analysis of clays. In *Crystal Structures of Clay Minerals and Their X-ray Identification*; Mineralogical Society of Great Britain and Ireland: Twickenham, UK, 1980; Volume 5, pp. 411–438.
66. Schultz, L.G. *Quantitative Interpretation of Mineralogical Composition X-ray and Chemical Data for the Pierre Shale*; Professional Paper; U.S. Geological Survey: Washington, DC, USA, 1964; pp. 1–31.
67. Nesbitt, H.W.; Young, G.M. Early Proterozoic climates and plate motions inferred from major element chemistry of lutites. *Nature* **1982**, *299*, 715–717. [[CrossRef](#)]
68. Nesbitt, H.; Young, G. Prediction of some weathering trends of plutonic and volcanic rocks based on thermodynamic and kinetic considerations. *Geochim. Cosmochim. Acta* **1984**, *48*, 1523–1534. [[CrossRef](#)]
69. McLennan, S. Weathering and Global Denudation. *J. Geol.* **1993**, *101*, 295–303. [[CrossRef](#)]
70. Fedo, C.M.; Nesbitt, H.W.; Young, G.M. Unraveling the effects of potassium metasomatism in sedimentary rocks and paleosols, with implications for paleoweathering conditions and provenance. *Geology* **1995**, *23*, 921–924. [[CrossRef](#)]
71. McLennan, S.M.; Hemming, S.; McDaniel, D.K.; Hanson, G.M. Geochemical approaches to sedimentation, provenance, and tectonics. In *Processes Controlling the Composition of Clastic Sediments*; Special Papers; Johnsson, M.J., Basu, A., Eds.; Geological Society of America: Boulder, CO, USA, 1993; Volume 284, pp. 21–40. [[CrossRef](#)]
72. Cullers, R.L. Implications of elemental concentrations for provenance, redox conditions, and metamorphic studies of shales and limestones near Pueblo, CO, USA. *Chem. Geol.* **2002**, *191*, 305–327. [[CrossRef](#)]
73. Bracciali, L.; Marroni, M.; Pandolfi, L.; Rocchi, S.; Arribas, J.; Critelli, S.; Johnsson, M. Geochemistry and petrography of Western Tethys Cretaceous sedimentary covers (Corsica and Northern Apennines): From source areas to configuration of margins. *Spec. Pap. Geol. Soc. Am.* **2007**, *420*, 73–93. [[CrossRef](#)]

74. Floyd, P.A.; Leveridge, B.E. Tectonic environment of the Devonian Gramscatho basin, south Cornwall: Framework mode and geochemical evidence from turbiditic sandstones. *J. Geol. Soc.* **1987**, *144*, 531–542. [[CrossRef](#)]
75. Bhatia, M.R.; Crook, K.A.W. Trace element characteristics of graywackes and tectonic setting discrimination of sedimentary basins. *Contrib. Miner. Pet.* **1986**, *92*, 181–193. [[CrossRef](#)]
76. Bhatia, M.R. Plate Tectonics and Geochemical Composition of Sandstones. *J. Geol.* **1983**, *91*, 611–627. [[CrossRef](#)]
77. Bhatia, M.R. Rare earth element geochemistry of Australian Paleozoic graywackes and mudrocks: Provenance and tectonic control. *Sediment. Geol.* **1985**, *45*, 97–113. [[CrossRef](#)]
78. Taylor, S.R.; McLennan, S.M. *The Continental Crust: Its Composition and Evolution*; Blackwell: Oxford, UK, 1985; 321p, ISBN-13: 978-0632011483.
79. Suttner, P.K.D.L.J. Alluvial Sandstone Composition and Paleoclimate, I. Framework Mineralogy. *J. Sediment. Res.* **1986**, *56*, 329–345. [[CrossRef](#)]
80. Cingolani, C.A.; Manassero, M.; Abre, P. Composition, provenance, and tectonic setting of Ordovician siliciclastic rocks in the San Rafael block: Southern extension of the Precordillera crustal fragment, Argentina. *J. S. Am. Earth Sci.* **2003**, *16*, 91–106. [[CrossRef](#)]
81. McLennan, S. Sedimentary silica on Mars. *Geology* **2003**, *31*, 315–318. [[CrossRef](#)]
82. Hegde, V.; Chavadi, V. Geochemistry of late Archaean metagreywackes from the Western Dharwar Craton, South India: Implications for provenance and nature of the Late Archaean crust. *Gondwana Res.* **2009**, *15*, 178–187. [[CrossRef](#)]
83. Abre, P.; Cingolani, C.; Zimmermann, U.; Cairncross, B.; Chemale, F. Provenance of Ordovician clastic sequences of the San Rafael Block (Central Argentina), with emphasis on the Ponón Trehué Formation. *Gondwana Res.* **2011**, *19*, 275–290. [[CrossRef](#)]
84. Stern, G.; Wagreich, M. Provenance of the Upper Cretaceous to Eocene Gosau Group around and beneath the Vienna Basin (Austria and Slovakia). *Swiss J. Geosci.* **2013**, *106*, 505–527. [[CrossRef](#)]
85. Hofmann, M.; Li, X.; Chen, J.; MacKenzie, L.; Hinman, N. Provenance and temporal constraints of the Early Cambrian Maotianshan Shale, Yunnan Province, China. *Gondwana Res.* **2016**, *37*, 348–361. [[CrossRef](#)]
86. Bibi, M.; Wagreich, M.; Iqbal, S.; Jan, I.U. Regional sediment sources versus the Indus River system: The Plio-Pleistocene of the Peshawar Basin (NW-Pakistan). *Sediment. Geol.* **2019**, *389*, 26–41. [[CrossRef](#)]
87. Bibi, M.; Wagreich, M.; Iqbal, S.; Gier, S.; Jan, I.U. Sedimentation and glaciations during the Pleistocene: Palaeoclimate reconstruction in the Peshawar Basin, Pakistan. *Geol. J.* **2020**, *55*, 671–693. [[CrossRef](#)]
88. Mange, M.A.; Maurer, H.F.W. *Heavy Minerals in Colour*; Chapman and Hall: London, UK, 1992; pp. 11–25.
89. Koroznikova, L.; Klutke, C.; McKnight, S.; Hall, S. The use of low-toxic heavy suspensions in mineral sands evaluation and zircon fractionation. *J. Afr. Inst. Min. Metall.* **2008**, *108*, 25–33.
90. Sorkhabi, R. How Much Oil in the Middle East? *GeoExPro* **2014**, *11*, 1–2014.
91. John, T.; Schenk, V.; Haase, K.; Scherer, E.; Tembo, F. Evidence for a Neoproterozoic ocean in south-central Africa from mid-oceanic-ridge-type geochemical signatures and pressure-temperature estimates of Zambian eclogites. *Geology* **2003**, *31*, 243–246. [[CrossRef](#)]
92. Basu, A. Petrology of Holocene fluvial sand derived from plutonic source rocks; implications to paleoclimatic interpretation. *J. Sediment. Res.* **1976**, *46*, 694–709. [[CrossRef](#)]
93. Gromet, L.; Haskin, L.A.; Korotev, R.L.; Dymek, R.F. The “North American shale composite”: Its compilation, major and trace element characteristics. *Geochim. Cosmochim. Acta* **1984**, *48*, 2469–2482. [[CrossRef](#)]
94. Nesbitt, H.W.; Young, G.M.; McLennan, S.; Keays, R. Effects of Chemical Weathering and Sorting on the Petrogenesis of Siliciclastic Sediments, with Implications for Provenance Studies. *J. Geol.* **1996**, *104*, 525–542. [[CrossRef](#)]
95. Rudnick, R.L.; Gao, S.; Holland, H.D.; Turekian, K.K. Composition of the continental crust. *Crust* **2003**, *3*, 1–64.
96. Hubert, J.F. A zircon-tourmaline-rutile maturity index and the interdependence of the composition of heavy mineral assemblages with the gross composition and texture of sandstones. *J. Sediment. Res.* **1962**, *32*, 440–450.
97. Garzanti, E.; Andò, S. Chapter 29 Plate Tectonics and Heavy Mineral Suites of Modern Sands. *Dev. Sedimentol.* **2007**, *58*, 741–763. [[CrossRef](#)]
98. Tucker, M.E. (Ed.) *Sedimentary Petrology: An Introduction to the Origin of Sedimentary Rocks*; John Wiley & Sons: Oxford, UK, 2009; p. 278.
99. Boggs, S., Jr.; Boggs, S. *Petrology of Sedimentary Rocks*; Cambridge University Press: Cambridge, UK, 2009; p. 600.
100. Condie, K.C. Another look at rare earth elements in shales. *Geochim. Cosmochim. Acta* **1991**, *55*, 2527–2531. [[CrossRef](#)]
101. Cox, R.; Lowe, D.R.; Cullers, R. The influence of sediment recycling and basement composition on evolution of mudrock chemistry in the southwestern United States. *Geochim. Cosmochim. Acta* **1995**, *59*, 2919–2940. [[CrossRef](#)]
102. Garver, J.I.; Scott, T.J. Trace elements in shale as indicators of crustal provenance and terrane accretion in the southern Canadian Cordillera. *GSA Bull.* **1995**, *107*, 440–453. [[CrossRef](#)]
103. Blake, J.M.; Peters, S.C.; Johannesson, K.H. Application of REE geochemical signatures for Mesozoic sediment provenance to the Gettysburg Basin, Pennsylvania. *Sediment. Geol.* **2017**, *349*, 103–111. [[CrossRef](#)]
104. Mukherjee, I.; Large, R.R.; Bull, S.; Gregory, D.G.; Stepanov, A.S.; Ávila, J.; Ireland, T.R.; Corkrey, R. Pyrite trace-element and sulfur isotope geochemistry of paleo-mesoproterozoic McArthur Basin: Proxy for oxidative weathering. *Am. Miner.* **2019**, *104*, 1256–1272. [[CrossRef](#)]
105. Little, S.H.; Vance, D.; Lyons, T.W.; McManus, J. Controls on trace metal authigenic enrichment in reducing sediments: Insights from modern oxygen-deficient settings. *Am. J. Sci.* **2015**, *315*, 77–119. [[CrossRef](#)]



106. Sweere, T.; Boorn, S.V.D.; Dickson, A.J.; Reichart, G.-J. Definition of new trace-metal proxies for the controls on organic matter enrichment in marine sediments based on Mn, Co, Mo and Cd concentrations. *Chem. Geol.* **2016**, *441*, 235–245. [[CrossRef](#)]
107. Kanhaiya, S.; Singh, B.P.; Singh, S. Mineralogical and Geochemical Behavior of Sediments Solely Derived from Bundelkhand Granitic Complex, Central India: Implications to Provenance and Source Rock Weathering. *Geochem. Int.* **2018**, *56*, 1245–1262. [[CrossRef](#)]
108. McLennan, S.; Taylor, S.; McCulloch, M.; Maynard, J. Geochemical and Nd Sr isotopic composition of deep-sea turbidites: Crustal evolution and plate tectonic associations. *Geochim. Cosmochim. Acta* **1990**, *54*, 2015–2050. [[CrossRef](#)]
109. Singer, A. The paleoclimatic interpretation of clay minerals in sediments—A review. *Earth Sci. Rev.* **1984**, *21*, 251–293. [[CrossRef](#)]
110. Dill, H.G. Kaolin: Soil, rock and ore: From the mineral to the magmatic, sedimentary and metamorphic environments. *Earth Sci. Rev.* **2016**, *161*, 16–129. [[CrossRef](#)]
111. Newman, S.; Macdougall, J.D.; Finkel, R.C. 230Th-238U disequilibrium in island arcs: Evidence from the Aleutians and the Marianas. *Nature* **1984**, *308*, 268–270. [[CrossRef](#)]
112. Worden, R.H.; Burley, S.D. Sandstone Diagenesis: The Evolution of Sand to Stone. *Sandstone Diagenesis* **2009**, *4*, 1–44.
113. Marfil, R.; La Iglesia, A.; Herrero, M.J.; Scherer, M.; Delgado, A. Clay mineral occurrence and burial transformations: Reservoir potential of the Permo-Triassic sediments of the Iberian Range. *Basin Res.* **2014**, *27*, 295–309. [[CrossRef](#)]
114. Mindszenty, A. Bauxites: Feedbacks of System Earth at Greenhouse times. *Geol. Croat.* **2016**, *69*, 79–87. [[CrossRef](#)]
115. Selvaraj, K.; Chen, C.A. Moderate Chemical Weathering of Subtropical Taiwan: Constraints from Solid-Phase Geochemistry of Sediments and Sedimentary Rocks. *J. Geol.* **2006**, *114*, 101–116. [[CrossRef](#)]
116. Bahlburg, H.; Dobrzinski, N.; Arnaud, E.; Halverson, G.P.; Shields-Zhou, G. Chapter 6 A review of the Chemical Index of Alteration (CIA) and its application to the study of Neoproterozoic glacial deposits and climate transitions. *Geol. Soc. Lond. Mem.* **2011**, *36*, 81–92. [[CrossRef](#)]
117. McLennan, S.M. Archean sedimentary rocks and the Archean mantle. In *Workshop on the Archean Mantle*; Technical Report; Aswal, L.D., Ed.; LPI: New York, NY, USA, 1989; Volume 89-05, pp. 57–59.
118. McLennan, S.; Taylor, S.R. Th and U in sedimentary rocks: Crustal evolution and sedimentary recycling. *Nat. Cell Biol.* **1980**, *285*, 621–624. [[CrossRef](#)]
119. McLennan, S.; Taylor, S.R. Sedimentary Rocks and Crustal Evolution: Tectonic Setting and Secular Trends. *J. Geol.* **1991**, *99*, 1–21. [[CrossRef](#)]
120. McLennan, S.M. Rare earth elements in sedimentary rocks: Influence of provenance and sedimentary processes. *Miner. Soc. Am. Rev. Mineral.* **1989**, *21*, 169–200.
121. Mange, M.A.; Wright, D.T. (Eds.) *Heavy Minerals in Use: Developments in Sedimentology*; Elsevier: Amsterdam, The Netherlands, 2007; p. 1283.
122. Sevastjanova, I.; Hall, R.; Alderton, D. A detrital heavy mineral viewpoint on sediment provenance and tropical weathering in SE Asia. *Sediment. Geol.* **2012**, *280*, 179–194. [[CrossRef](#)]
123. Rino, S.; Kon, Y.; Sato, W.; Maruyama, S.; Santosh, M.; Zhao, D. The Grenvillian and Pan-African orogens: World's largest orogenies through geologic time, and their implications on the origin of superplume. *Gondwana Res.* **2008**, *14*, 51–72. [[CrossRef](#)]
124. Stern, R.J.; Johnson, P. Continental lithosphere of the Arabian Plate: A geologic, petrologic, and geophysical synthesis. *Earth Sci. Rev.* **2010**, *101*, 29–67. [[CrossRef](#)]
125. Heikal, M.T.S.; Al-Khirbash, S.A.; Hassan, A.M.; Al-Kotbah, A.M.; Al-Selwi, K.M. Lithostratigraphy, deformation history, and tectonic evolution of the basement rocks, Republic of Yemen: An overview. *Arab. J. Geosci.* **2013**, *7*, 2007–2018. [[CrossRef](#)]
126. Whitehouse, M.J.; Windley, B.F.; Stoesser, D.B.; Al-Khirbash, S.; Ba-Bttat, M.A.; Haider, A. Precambrian basement character of Yemen and correlations with Saudi Arabia and Somalia. *Precambrian Res.* **2001**, *105*, 357–369. [[CrossRef](#)]
127. Stampfli, G.; Marcoux, J.; Baud, A. Tethyan margins in space and time. *Palaeogeogr. Palaeoclim. Palaeoecol.* **1991**, *87*, 373–409. [[CrossRef](#)]
128. Pillevuit, A. Les Blocs exotiques du Sultanat d'Oman, évolution paléogéographique d'une marge passive flexurale. *Mémoires Géologie Lausanne* **1993**, *17*, 1–249.
129. Wopfner, H. Pangean depositional sequences between Karoo and Lut. In *Geoscientific Research in Northeast Africa*; Balkema, A.A., Thorweihe, U., Schandelmeier, H., Eds.; Brookfield: Rotterdam, The Netherlands, 1993; pp. 189–195.
130. Jin, X. Permo-Carboniferous sequences of Gondwana affinity in Southwest China and their paleogeographic implications. *J. Asian Earth Sci.* **2002**, *20*, 633–646.
131. Ghani, H.; Sobel, E.R.; Zeilinger, G.; Glodny, J.; Zapata, S.; Irum, I. Palaeozoic and Pliocene tectonic evolution of the Salt Range constrained by low-temperature thermochronology. *Terra Nova* **2021**, *33*, 293–305. [[CrossRef](#)]
132. Sciunnach, D.; Garzanti, E. Sedimentary record of Late Paleozoic rift and break-up in Northern Gondwana: A case history from the Thini Chu Group and Tamba-Kurkur Formation (Dolpo Tethys Himalaya, Nepal). *Geodin. Acta* **1996**, *9*, 41–56. [[CrossRef](#)]
133. Sciunnach, D.; Garzanti, E. Detrital chromian spinels record tectono-magmatic evolution from Carboniferous rifting to Permian spreading in Neotethys (India, Nepal and Tibet). In *From Rifting to Drifting in Present-Day and Fossil Ocean Basins*; Messiga, B., Tribuzio, R., Eds.; Ofioliti: Pisa, Italy, 1997; pp. 101–110.
134. Jin, Y.; Shen, S.Z.; Zhu, Z.; Mei, S.; Wang, W. The Selong section, candidate of the global stratotype and section, and point of the Permian–Triassic boundary. In *The Palaeozoic–Mesozoic Boundary Candidates of Global Stratotype Section and Point of the Permian–Triassic Boundary*; Yin, H.F., Ed.; China University of Geosciences: Beijing, China, 1996; pp. 127–137.

135. Wignall, P.B.; Newton, R. Contrasting Deep-water Records from the Upper Permian and Lower Triassic of South Tibet and British Columbia: Evidence for a Diachronous Mass Extinction. *PALAIOS* **2003**, *18*, 153–167. [[CrossRef](#)]
136. von Rad, U.; Exon, N.F.; Boyd, R.; Haq, B.U. Mesozoic paleoenvironment of the rifted margin off NW Australia (ODP Legs 122/123). In *American Geophysical Union Monograph*; Duncan, R.A., Rea, D.K., Kidd, R.B., von Rad, U., Weissel, J.K., Eds.; American Geophysical Union: Washington, DC, USA, 1992; Volume 70, pp. 157–184. [[CrossRef](#)]
137. Garzanti, E.; Le Fort, P.; Sciunnach, D. First report of Lower Permian basalts in South Tibet: Tholeiitic magmatism during break-up and incipient opening of Neotethys. *J. Asian Earth Sci.* **1999**, *17*, 533–546. [[CrossRef](#)]
138. Biswas, S. Regional tectonic framework, structure and evolution of the western marginal basins of India. *Tectonophysics* **1987**, *135*, 307–327. [[CrossRef](#)]
139. Mukhopadhyay, G.; Mukhopadhyay, S.K.; Roychowdhury, M.; Parui, P.K. Stratigraphic correlation between different Gondwana Basins of India. *J. Geol. Soc. India* **2010**, *76*, 251–266. [[CrossRef](#)]
140. Brown, B.J.; Muller, R.D.; Gaina, C.; Struckmeyer, H.I.M.; Stagg, H.M.J.; Symonds, P.A. Formation and evolution of Australian passive margins: Implications for locating the boundary between continental and oceanic crust. *Spec. Pap. Geol. Soc. Am.* **2003**, *372*, 223–244.
141. Green, P.F.; Japsen, P.; Chalmers, J.A.; Bonow, J.M.; Duddy, I.R. Post-breakup burial and exhumation of passive continental margins: Seven propositions to inform geodynamic models. *Gondwana Res.* **2018**, *53*, 58–81. [[CrossRef](#)]
142. Martin, A.J. A review of Himalayan stratigraphy, magmatism, and structure. *Gondwana Res.* **2017**, *49*, 42–80. [[CrossRef](#)]
143. Heron, A.M. The geology of central Rajputana. *Mem. Geol. Soc. India* **1953**, *79*, 389.
144. Sisodia, M.S.; Chauhan, D.S. *Indian Precambrian*; Paliwal, B.S., Ed.; Scientific Publisher: Jodhpur, India, 1998; pp. 171–182.
145. Bhushan, S.K. Classification of Malani Igneous Suite. *Geol. Surv. India Spec. Public* **1984**, *12*, 199–205.
146. Di Giulio, A.; Amadori, C.; Mueller, P.; Langone, A. Role of the Down-Bending Plate as a Detrital Source in Convergent Systems Revealed by U–Pb Dating of Zircon Grains: Insights from the Southern Andes and Western Italian Alps. *Minerals* **2020**, *10*, 632. [[CrossRef](#)]
147. Burley, S.; Worden, R. (Eds.) *Sandstone Diagenesis: Recent and Ancient*; Wiley-Blackwell: Hoboken, NJ, USA, 2009; Volume 24, p. 650.
148. Walderhaug, O. Temperatures of Quartz Cementation in Jurassic Sandstones from the Norwegian Continental Shelf—Evidence from Fluid Inclusions. *J. Sediment. Res.* **1994**, *64*, 311–323. [[CrossRef](#)]
149. Primmer, T.J.; Cade, C.A.; Evans, J.; Gluyas, J.G.; Hopkins, M.S.; Oxtoby, N.H.; Smalley, S.; Warren, E.A.; Worden, R.H. Global patterns in sandstone diagenesis: Their application to reservoir quality prediction for petroleum exploration. In *Reservoir Quality Prediction in Sandstones and Carbonates*; Kupecz, J.A., Gluyas, J., Bloch, S., Eds.; American Association of Petroleum Geologists: Tulsa, OK, USA, 1997; pp. 61–77, Memoir 69.
150. Worden, R.; Morad, S. *Quartz Cementation in Sandstones*; Special Publication 29, International Association of Sedimentologists; Blackwell Science: Oxford, UK, 2000; p. 342.